Crystal plasticity simulation of in-grain microstructural evolution during large deformation of IF-steel

Sedighiani, Karo; Traka, Konstantina; Roters, Franz; Sietsma, Jilt; Raabe, Dierk; Diehl, Martin

DOI
10.1016/j.actamat.2022.118167

Publication date
2022

Document Version
Final published version

Published in
Acta Materialia

Acta Materialia 237 (2022) 118167

Contents lists available at ScienceDirect

Acta Materialia

journal homepage: www.elsevier.com/locate/actamat

Full length article

Crystal plasticity simulation of in-grain microstructural evolution during large deformation of IF-steel

Karo Sedighiani[a,b,*], Konstantina Traka[a,b], Franz Roters[a], Jilt Sietsma[b], Dierk Raabe[a], Martin Diehl[c,d]

[a] Max-Planck-Institut für Eisenforschung, Max-Planck-Str. 1, Düsseldorf 40237, Germany
[b] Department of Materials Science and Engineering, Delft University of Technology, Mekelweg 2, CD Delft 2628, The Netherlands
[c] Department of Materials Engineering, KU Leuven, Kasteelpark Arenberg 44, Leuven 3001, Belgium
[d] Department of Computer Science, KU Leuven, Celestijnenlaan 200 A, Leuven 3001, Belgium

ARTICLE INFO

Article history:
Received 2 March 2022
Revised 16 June 2022
Accepted 11 July 2022
Available online 15 July 2022

Keywords:
Crystal plasticity
Microtexture
Shear bands
Dislocation density
Polycrystalline materials
DAMASK

ABSTRACT

High-resolution three-dimensional crystal plasticity simulations are used to investigate deformation heterogeneity and microstructure evolution during cold rolling of interstitial free (IF-) steel. A Fast Fourier Transform (FFT)-based spectral solver is used to conduct crystal plasticity simulations using a dislocation-density-based crystal plasticity model. The in-grain texture evolution and misorientation spread are consistent with experimental results obtained using electron backscatter diffraction (EBSD) experiments. The crystal plasticity simulations show that two types of strain localization features develop during the large strain deformation of IF-steel. The first type forms band-like areas with large strain accumulation that appear as river patterns extending across the specimen. In addition to these river-like patterns, a second type of strain localization with rather sharp and highly localized in-grain shear bands is identified. These localized features are dependent on the crystallographic orientation of the grain and extend within a single grain. In addition to the strain localization, the evolution of in-grain orientation gradients, misorientation features, dislocation density, kernel average misorientation, and stress in major texture components are discussed.

1. Introduction

Plastic deformation of polycrystalline metals is significantly heterogeneous in terms of strain, stress, and crystal reorientation. Characterization and understanding of these deformation heterogeneities and the associated microstructural evolution during plastic deformation play a critical role in identifying the underlying mechanisms behind many physical phenomena. For instance, a thorough physical understanding of the mechanisms leading to recrystallization is not feasible without properly characterizing microstructural evolution during plastic deformation [1–7]. Moreover, damage formation, fracture, and failure in metals are also often related to deformation localization and microstructures formed during deformation [8–11]. Besides, the material properties of crystalline materials depend on the microstructures developing during the deformation including crystallographic texture [12,13]. As a result, over the past years, a considerable amount of attention has been devoted to understand and characterize the intragranular deformation heterogeneity and microstructural evolution during plastic deformation [14–21].

Deformation microstructures are mainly quantified using experimental techniques such as scanning [22–26] and transmission [27,28] electron microscope based techniques. Choi and Jin [22], Choi and Cho [23] used electron backscatter diffraction (EBSD) analysis to examine the orientation dependency of the stored energy of deformed grains in cold-rolled low carbon steels. Allain-Bonasso et al. [25] studied the effect of orientation distributions and grain size on the development of deformation heterogeneities during tensile deformation of interstitial free (IF-) steel by EBSD. Wang et al. [26] investigated shear band formation in cold-rolled Ta-2.5W alloy at various thickness reduction levels using EBSD analysis. Li et al. [27] investigated the microstructural evolution during cold rolling of IF-steel at different thickness reductions using scanning and transmission electron microscope techniques.

Despite the extensive amount of knowledge that can be developed from experimental studies, most experimental techniques suffer from several drawbacks: (i) The microstructure and micro-

* Corresponding author.
E-mail address: k.sedighiani@tudelft.nl (K. Sedighiani).

https://doi.org/10.1016/j.actamat.2022.118167

texture can be characterized solely based on the specimen surface, and determining the variation of microstructure through the thickness is only possible using destructive or highly advanced, expensive approaches. As a result, the actual neighboring and boundary conditions of the material points cannot be precisely determined. (ii) It is difficult to track the region of interest, especially during large deformation. (iii) A large number of experiments are required to acquire complete knowledge of the deformation history, which is extremely time-consuming and economically inefficient. (iv) The experimental procedures usually contain uncertainty due to sensitivity to sample contamination and random errors.

Crystal plasticity simulations [29] have been established as an alternative to model and quantify deformation processes at the microstructural level and the associated complex mechanical fields [30–37]. These models are developed based on physical mechanisms such as glide of dislocations on preferred slip systems and the interaction of dislocations with various defects. Crystal plasticity simulations have been compared with experimental data in several works. For instance, Raabe et al. [38] compared the spatial distribution of the plastic strain from channel-die experiments with crystal plasticity simulations for a sample of pure aluminum with 18 grains after an 8% sample thickness reduction. However, comparisons between simulations and experiments are mostly limited to small/moderate strains (strains less than 0.4) [38,39] or simple microstructures (e.g. bicrystals) [40–43].

Problems involving the deformation of solid materials are usually formulated in a Lagrangian context, in which the mesh is attached to the deformable body and deforms with a change in the material's shape. As a result, the mesh gets distorted due to the heterogeneity of the deformation [44,45]. When the mesh distortion becomes too large, the simulation fails to converge. At the same time, modeling of in-grain localized deformation features requires a high-resolution crystal plasticity simulation, even up to hundreds of thousands of elements per crystal [44,46]. A higher simulation resolution allows capturing more detailed localized deformation features, which results in earlier mesh convergence issues.

This paper presents a computational study to investigate the evolution of in-grain deformation heterogeneity during cold rolling of IF-steel over a wide range of strains up to 77% thickness reduction. The large-deformation crystal plasticity simulations are conducted using the remeshing technique proposed by Sedighiani et al. [44]. This approach enables conducting high-resolution large-deformation crystal plasticity simulations and overcoming the associated mesh distortion problem due to the strain localization. The in-grain orientation spreads obtained using simulation are compared with two EBSD measurements performed on a cold-rolled IF steel sample after 77% thickness reduction. In addition, the orientation dependency of deformation heterogeneity, strain localization, and dislocation evolution are numerically investigated over a wide range of strains.

2. Microstructure evolution in steels

In bcc metals, dislocation slip occurs along the $\langle 111 \rangle$ direction, where the slip plane can be {110}, {112}, and at higher temperatures also {123} [47,48]. The lattice rotates due to the shear strain and reaches a preferred orientation based on the loading conditions and the initial orientation of the lattice. There are numerous works devoted to studying the evolution of texture in bcc metals and especially steel [27,45,49–57]. The rolling texture in bcc metals belongs mainly to two families of α (RD$\|\langle 110 \rangle$) and γ (ND$\|\langle 111 \rangle$) fibers. In general, the rolling texture developed in bcc metals is noticeably affected by the degree of deformation. By increasing thickness reductions, the main features of the texture remain similar. However, at large strains, the α-fiber becomes stronger and more prominent at the expense of weakening the γ-fiber[51].

The evolution of the in-grain microstructure in bcc metals has been a motivation for many experimental works [25,27,50,51,54,57]. It was found that crystals with an initial rotated cube orientation $\{001\}\langle 110 \rangle$ show minimal deformation heterogeneity [51,52]. The deformation heterogeneity increases for orientations further along the α-fiber, such as $\{112\}\langle 110 \rangle$, and the hard orientations of $\{111\}\langle 110 \rangle$ and $\{110\}\langle 110 \rangle$ contain the largest internal misorientations [58]. However, the soft α-fiber orientations also sometimes show texture dispersion when they are located near a hard grain [51,59]. Generally, a stronger tendency to form in-grain misorientation spread is observed in the γ-fiber compared to the α-fiber.

Under plane-strain deformation, a soft grain cannot store energy alone by concentrating the deformation into localized shears [60]. On the contrary, the formation of in-grain shear bands for hard grains is energetically more favorable than deforming the grain homogeneously under large stress boundary conditions. Therefore, in-grain shear bands are observed more frequently in hard γ-fiber orientations, whereas intergranular deformation heterogeneities are more common in softer α-fiber orientations [51]. In-grain shear bands are more prevalent in $\{111\}\langle 112 \rangle$ orientations [61,62]. In steel, they are most frequently formed at an angle of approximately 35° with the rolling direction [60,62,63]. These bands can be explained by their high degree of texture softening [64]. Barnett [62] observed that for $\{111\}\langle 112 \rangle$ oriented grains, the orientation inside the in-grain shear bands rotate toward the texture component of $\{554\}\langle 225 \rangle$.

Table 1
The chemical composition of the IF-steel considered in this study.

element	C	Mn	S	Ti	N	Al	Cr	Fe
wt. (%)	0.002	0.095	0.006	0.045	0.002	0.05	0.02	balance

3. Experimental methods

The material used in the present study is an IF-steel with chemical composition as given in Table 1. The initial microstructure and crystallographic texture of the material before cold rolling were measured on the RD-ND (rolling direction-normal direction) plane perpendicular to the transverse direction (TD) using electron backscatter diffraction (EBSD), see [65] for more information. The grain structure is almost completely equiaxed, and the material exhibits a mild texture commonly observed for hot-rolled IF steel.

We performed two EBSD measurements on two nearby areas of the industrially cold-rolled IF-steel sample subjected to 77% thickness reduction ($\varepsilon = 1.47$). The two scanning areas are located at the mid-thickness of the rolling plane (ND-RD plane). Therefore, these areas experience a near plane-strain compression deformation mode, i.e. shear deformation modes are negligible. The first EBSD map of a scan area of 600 μm$\times$600 μm was measured with a step size of 0.3 μm. The second EBSD map of a scan area of 594 μm $\times$438 μm was measured with a step size of 0.6 μm. Standard metallographic techniques were used to prepare the specimens for characterization. Analysis of the EBSD data was performed using the TSL OIM software.

4. Crystal plasticity simulations

In the computational example presented in this study, we use a high-resolution RVE consisting of 36 grains to investigate the deformation patterning and misorientation features evolving during large strain deformation. The crystallographic orientations of the

Table 2
Model parameters of IF-steel used for crystal plasticity simulations.

variable	description	units	value
ρ_0^α	initial mobile dislocation density	m/m^3	1.0×10^{12}
ρ_{d0}^α	initial dipole dislocation density	m/m^3	1.5×10^{12}
v_0	dislocation glide velocity pre-factor	m/s	1.4×10^3
ΔF	activation energy for dislocation glide	J	1.57×10^{-19}
p	p-exponent in glide velocity	–	0.325
q	q-exponent in glide velocity	–	1.55
τ_0^*	short-range barriers strength at 0 K	MPa	454
C_λ	parameter controlling dislocation mean free path	–	50
C_{anni}	coefficient for dislocation annihilation	–	2

grains are sampled from the EBSD map of the undeformed hot-rolled sample (see [65] for more information) using the approach presented by Eisenlohr and Roters [66]. The RVE is subjected to plane-strain compression at a strain rate of 100 s^{-1} up to a total thickness reduction of 77% ($\varepsilon = 1.47$). The initial number of elements at the beginning of the deformation is $80 \times 48 \times 320$, i.e. around 34000 elements per grain on average. The number of elements is gradually increased to $1280 \times 48 \times 320$ during the deformation using a multi-step mesh refinement method as described in Section 4.1. Therefore, at the final stages of the deformation, each grain is discretized using around 550000 elements. Considering an average initial grain size of 50 μm, the approximate element sizes at the beginning and at the end of the simulation would be 1.6 μm and 0.4 μm, respectively. Such a large number of elements per grain allows for predicting the development of a strain gradient and deformation heterogeneities within the grain.

We use a Fast Fourier Transform (FFT) based spectral method [67,68] implemented in DAMASK [69] to conduct the crystal plasticity simulations using a dislocation-density-based constitutive law [65,70]. The material parameters used in this study are based on the parameters identified in [65] for IF-steel using the approach presented in [71]. However, the hardening-related parameters (C_λ and C_{anni}) are revised based on the hardening behavior of the material at large strains, see Table 2.

4.1. Remeshing procedure

We use a remeshing technique presented by Sedighiani et al. [44] to overcome the mesh distortion problem in the high-resolution crystal plasticity simulations. This employed method is based on replacing the distorted mesh with a new undistorted mesh. The variables from the deformed stage are mapped onto the newly created mesh using a nearest-neighbor mapping algorithm. Finally, the simulation is restarted as a new simulation in which the initial state is set based on the last deformation state that had been reached.

During large deformation, the elements' aspect ratio, i.e. the ratio of the element size in the stretching direction to the element size in the compression direction, can become very large. Extensively elongated elements introduce errors in the simulation and, more importantly, can prevent strain localization. A multi-step mesh refinement method is used for updating the mesh density during the deformation at each remeshing step [44]. The idea behind this approach is to keep the number of elements in the compression direction constant and adjust the number of elements in the stretching direction accordingly to keep the elements close to a cubic shape. The multi-step mesh refinement approach leads to a gradual rise in the number of elements and the simulation resolution during the deformation. Keeping the number of elements in the most compressed direction constant ensures a minimum information loss during mapping with a minimal increase in the number of simulation points [44].

5. Results and discussion

We use a combined simulation and experimental study to investigate the deformation heterogeneity developed within grains at large strains. For this purpose, the results from the large-deformation crystal plasticity simulation with high resolution (Section 4) are compared with the results from two EBSD measurements (see Section 3).

5.1. Texture evolution

Fig. 1 a shows the inverse pole figure (IPF) color maps parallel to the loading (vertical) direction in the mid-surface of the 3D simulation for different thickness reductions. The 3D IPF color map for the same RVE after 77% thickness reduction is shown in Fig. 1b. The $\varphi_2 = 45^\circ$ section of the orientation distribution function for the 3D simulation is shown in Fig. 1c. Plastic deformation leads to changes in the grains' orientation and the development of deformation textures. The simulation results show that a strong α-fiber and a slightly weaker γ-fiber are developed after 77% thickness reduction. Figs. 3a and 4a show the IPF color map parallel to the loading (vertical) direction for two EBSD measurements on two nearby areas of the industrially cold-rolled IF-steel sample subjected to 77% thickness reduction (see Section 3). The corresponding $\varphi_2 = 45^\circ$ sections of the orientation distribution function for these two EBSD maps are shown in Figs. 3d and 4d, respectively.

Despite some differences in the predicted texture, there is a good agreement between the three sets of results. The first EBSD measurement shows almost the same strength for the two fibers, while the second EBSD data shows a strong α-fiber and a much weaker γ-fiber. The main reason for the different observations between the three sets of the results is that neither of the data sets is statistically fully representative of the material microstructure. It is challenging to conduct simulations and experiments at such resolutions in a way that full statistical representation of the material microstructure is obtained. Therefore, statistical differences are expected between the three sets of results, i.e. the two EBSD measurements and the simulation result.

5.2. Misorientation spread

This section investigates the deformation heterogeneity in terms of misorientation spread developed within the RVE. For this purpose, the data is divided into low KAM (kernel average misorientation) regions, i.e. points whose KAM value belongs to the lower 20% of the data distribution, and high KAM regions, points whose KAM value belongs to the higher half of the data distribution. For calculating the KAM of a point, the disorientation, i.e. the misorientations considering the cubic symmetry of the material, to all first-order neighboring points is calculated. Then, the average value is calculated. The IPF color maps parallel to the loading (vertical) direction for low KAM and high KAM regions are shown respectively in Fig. 2b and c, and the corresponding orientation density maps are shown respectively in Fig. 2e and f. For the sake of comparison, the IPF color map and the corresponding orientation density map of the full mid-surface are shown respectively in Fig. 2a and d.

The tendency to form in-grain misorientation spread is smaller in crystals belonging to the α-fiber. Specifically, grains close to the rotated cube orientation, $\{001\}\langle 110\rangle$, show minimal deformation heterogeneity, i.e. a very small misorientation spread. This is in accordance with the experimental observations (e.g. [51,52]) that, for this texture component, the orientation does not change noticeably during the rolling deformation (the in-grain orientation remains below 15° misorientation), and a uniform microstructure

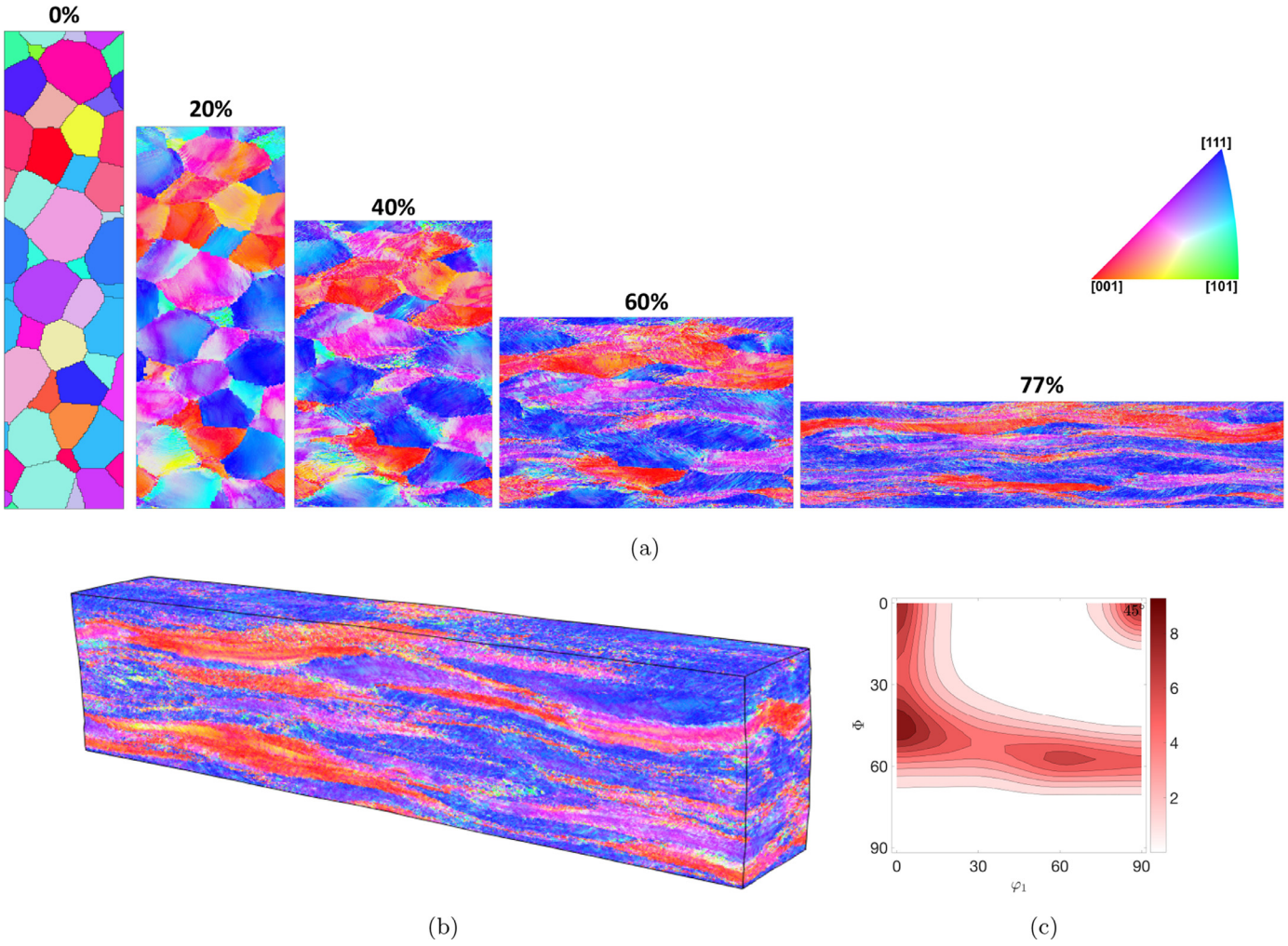

Fig. 1. (a) IPF color maps parallel to the loading (vertical) direction in the mid-surface of the 3D simulation at different thickness reductions. (b) The 3D IPF color maps and (c) Orientation density f(g) maps ($\varphi_2 = 45^\circ$) for the same RVE after 77% thickness reduction.

without significant orientation gradients is formed during deformation. The inverse Brass orientation, {112}⟨110⟩, shows similar behavior, and grains close to this crystallographic orientation show generally small misorientation spread. However, the in-grain misorientation spread is slightly larger compared to that of the rotated cube component. In general, the deformation heterogeneity increases for orientations further along the α-fiber, such as {112}⟨110⟩ and {111}⟨110⟩. The crystal plasticity simulation shows a stronger tendency to form in-grain misorientation spread in the γ-fiber compared to the α-fiber. The results from the two EBSD measurements confirm similar behavior, as shown in Fig. 3, 4. Regions with small deformation heterogeneity and misorientation spread belong mainly to the α-fiber, while the components belonging to the γ-fiber show the strongest misorientation spread. These observations show significant similarities with experimentally reported results in the literature for bcc metals, e.g. [49,51,52,54,72].

5.3. In-grain orientation gradients

In this section, we investigate the deformation heterogeneity in terms of in-grain orientation gradients (orientation variations within a grain). We quantify the in-grain deformation heterogeneity using grain orientation spread (GOS) and grain average misorientation (GAM). The GOS is the average of disorientation angles of all points within a grain to the grain mean orientation:

$$\mathrm{GOS_i} = \frac{1}{N_i}\sum_{j=1}^{N_i}\omega_{ij}, \tag{1}$$

where N_i stands for the number of points belonging to grain i, and ω_{ij} is the disorientation angle between point j and grain i's mean orientation considering the cubic symmetry of the material. The GAM is the average of the KAM for all points within a grain:

$$\mathrm{GAM_i} = \frac{1}{N_i}\sum_{j=1}^{N_i}\mathrm{KAM}_j, \tag{2}$$

The GAM parameter can be seen as a local measure for the orientation variation inside the grains. Larger GOS and GAM values reflect a higher degree of plastic deformation heterogeneity.

Fig. 5 a shows the GOS and GAM values for different grains. The grains are defined and numbered based on the initial microstructure before deformation as shown in Fig. 5b. The inverse pole figure distribution maps with respect to the loading direction (z) and stretching direction (x) for a few selected grains are shown in Fig. 6. The large reorientation spread for the grains reveals that in addition to the initial orientation, other factors like spatial constraints of neighboring points also play a crucial role. This is because the resolved shear stresses on various slip planes are determined by the compression load combined with the spatial constraints applied by the neighboring material. In general, the

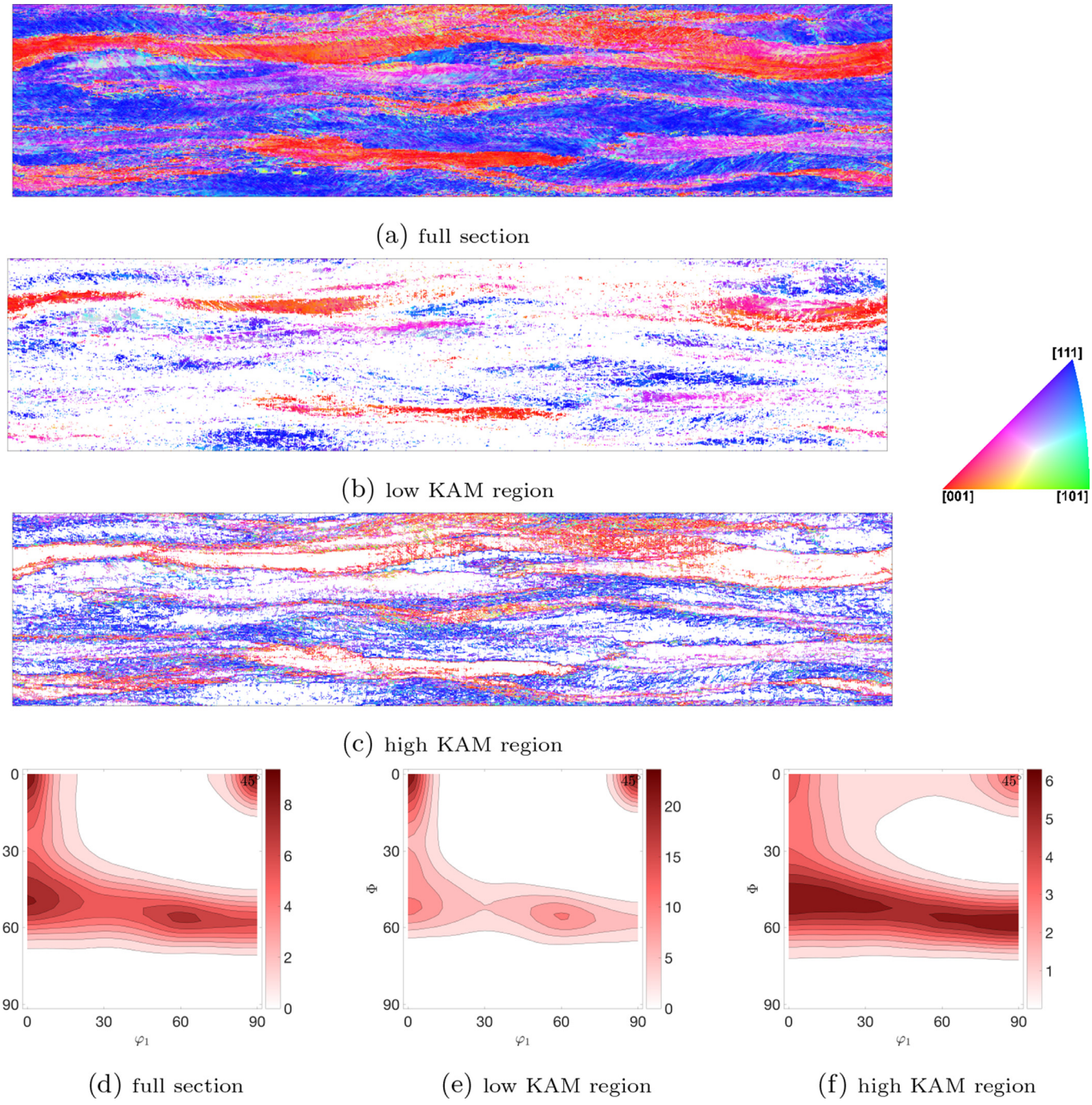

Fig. 2. Simulation results showing the low and high KAM regions in the mid-surface of the 3D simulation after 77% thickness reduction. (a–c) IPF color maps parallel to the loading (vertical) direction, (d–f) orientation density f(g) maps obtained from the ODF section $\varphi_2 = 45^\circ$.

GOS and the GAM values are noticeably smaller in grains belonging to the α-fiber (e.g. grains 18, 29, 31, 32, and 33) than in grains belonging to the γ-fiber (e.g. grains 3, 4, 13, and 35). The smallest values of GOS and GAM belong to grains with orientations close to the rotated cube orientation.

Fig. 7 shows the correlation between the GOS and the GAM with volume fraction of various texture components. There is a strong negative correlation between the volume fraction of the points belonging to the α-fiber with GOS and GAM, which means that a more uniform microstructure without significant orientation gradients is formed in grains with a larger volume fraction of α-fiber orientations. On the other hand, there is a weak positive correlation between the volume fraction of the γ-fiber with GOS and GAM, which implies noticeable variations in the orientation spread for grains with a similar fraction of orientations belonging to the γ-fiber. For example, the GOS & GAM values for grains 6 and 15 are respectively 14.2 & 9.8 and 34.0 & 15.1. This result indicates that local effects and the local stress field considerably affect the reorientation of crystal points rotating towards the γ-fiber. Therefore, altering the grain shape or orientation of a neighboring grain can suppress or promote grain fragmentation in these crystals more strongly than in the α-fiber grains. Between the γ-fiber components, we observed that the volume fraction of $\{554\}\langle225\rangle$ component has the strongest correlation with the GOS and GAM.

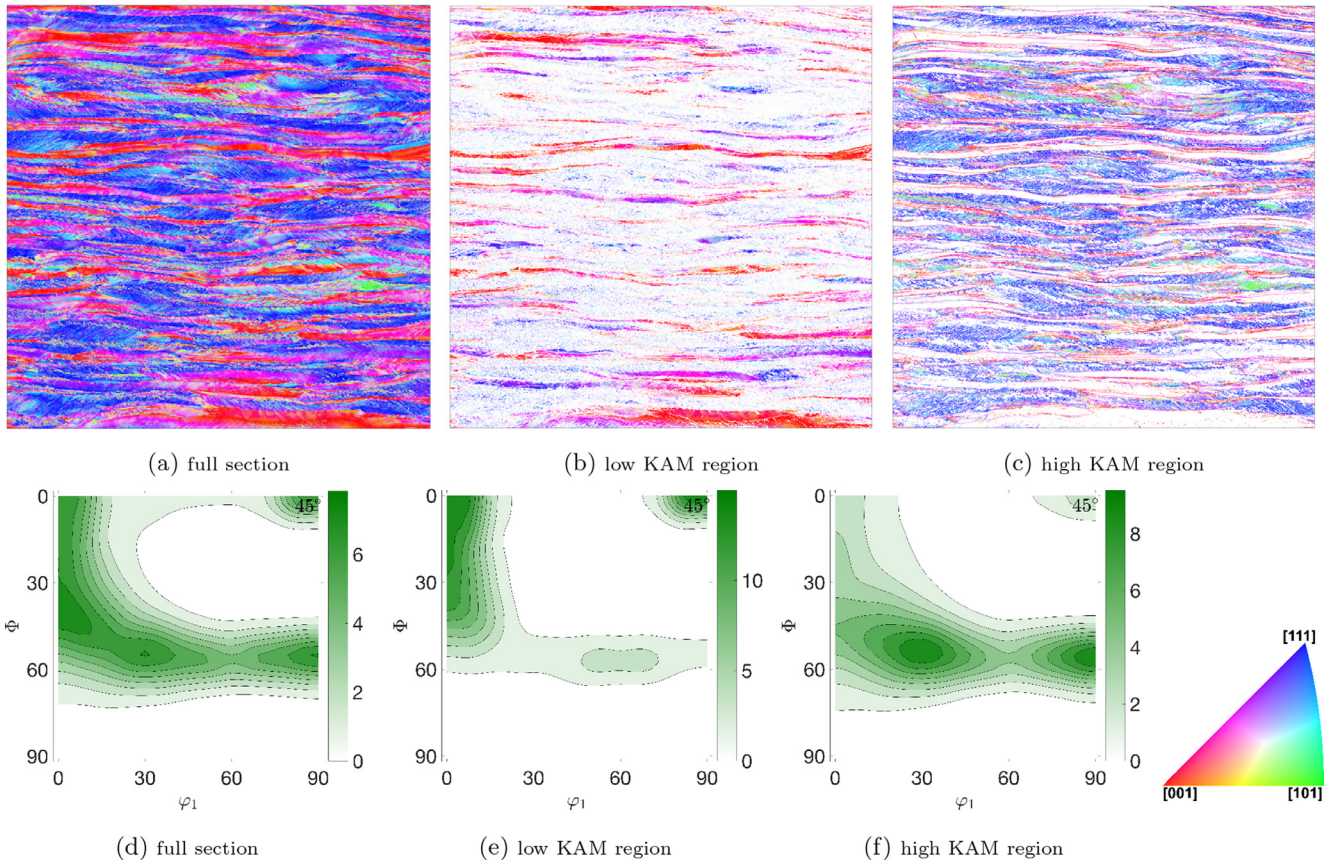

Fig. 3. Results showing low and high KAM regions of EBSD measurement 1 for a 600 μm × 600 μm scan area. (a–c) IPF color maps parallel to the loading (vertical) direction, (d–f) orientation density f(g) maps obtained from the ODF section $\varphi_2 = 45^\circ$.

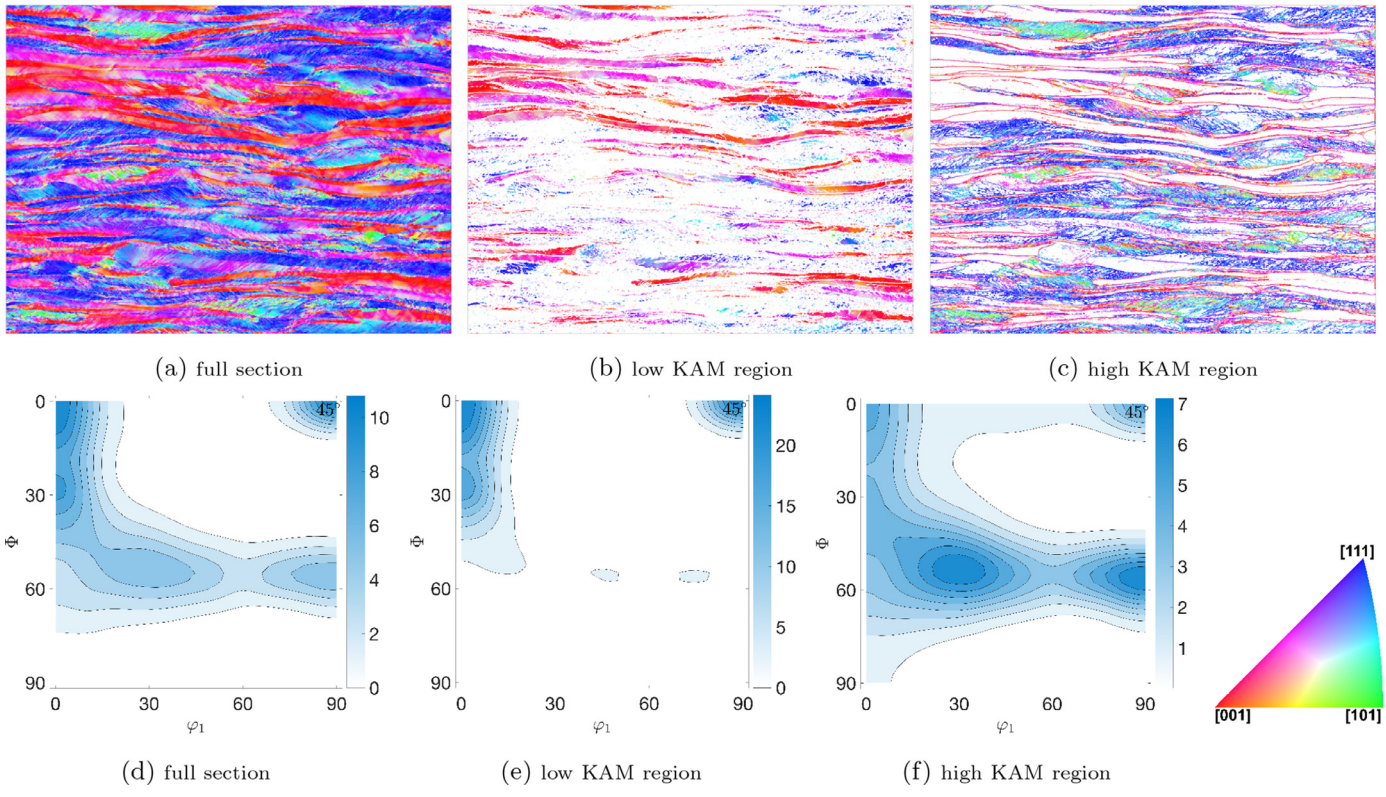

Fig. 4. Results showing low and high KAM regions of EBSD measurement 2 for a 594 μm × 438 μm scan area. (a–c) IPF color maps parallel to the loading (vertical) direction, (d–f) orientation density f(g) maps obtained from the ODF section $\varphi_2 = 45^\circ$.

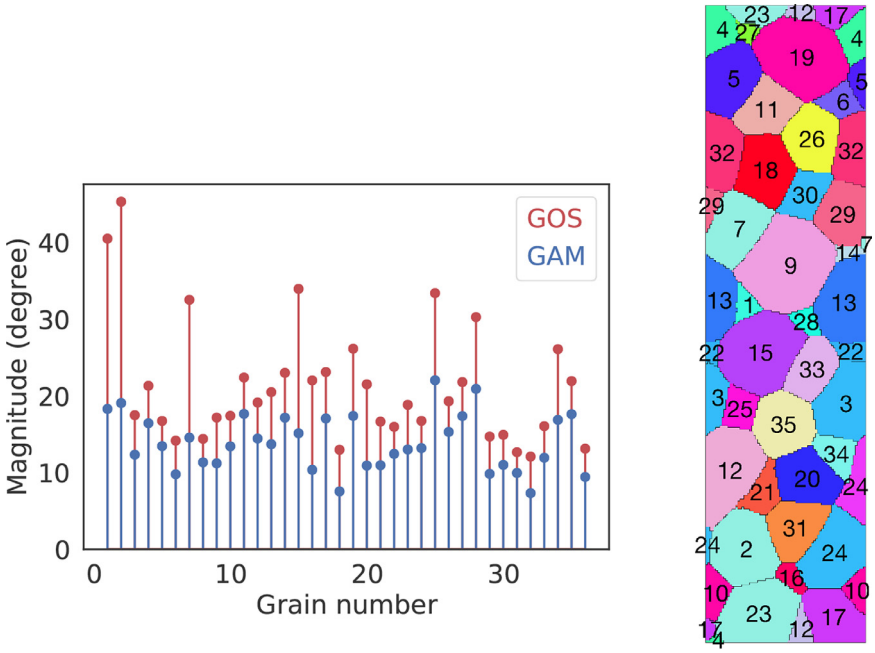

Fig. 5. (a) GOS and GAM for all individual grains. (b) Grains are defined and numbered based on the initial microstructure before deformation.

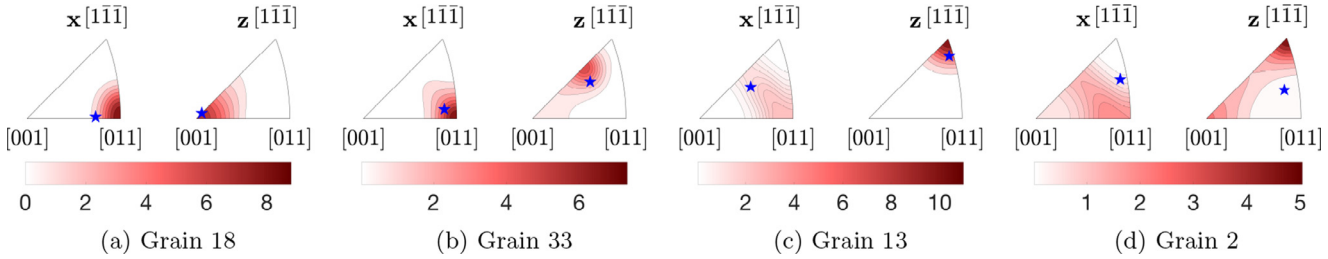

Fig. 6. Inverse pole figure distribution map with respect to the loading direction (z) and stretching direction (x) for four selected grains. (a) A Grain close to the rotated cube orientation with minimal deformation heterogeneity; (b) A grain belonging to the α-fiber showing a small tendency to form in-grain misorientation spread; (c) A grain belonging to the γ-fiber showing a strong tendency to form in-grain misorientation spread compared to the α-fiber; (d) A grain fragmented into regions of distinctly different orientations. The grains are defined based on the initial microstructure before deformation (see Fig. 5b), and the blue stars show the initial orientations. (For interpretation of the references to colour in this figure legend, the reader is referred to the web version of this article.)

On the other hand, the volume fraction of $\{111\}\langle 110\rangle$ has the weakest correlation with the GOS and GAM. These outputs indicate that the in-grain orientation spread is orientation-dependent. The analysis presented here is based on how the initially uniform grains reorient during plastic deformation and form in-grain orientation gradients. It is one of the main advantages of simulations to allow simple tracking of the reorientation history for all points, while such an analysis for experimental methods is often impossible.

There is a significant difference between the GOS and GAM values for some grains, e.g. grain 2. A 2D section of grain 2 at the mid-surface is shown in Fig. 8. As can be seen, this grain has been fragmented into two regions of distinctly different orientations. As a result, the misorientation angle to the grain mean orientation is noticeably large for most points within the grain. However, since the GAM measures local variation in the orientation, it captures the bifurcation. For such cases, looking at the GOS alone may be misleading.

5.4. Shear localization

This section investigates the evolution of intergranular and intragranular shear localization during the deformation of the IF-steel over a wide strain range. Fig. 9 shows the development of different variables (i.e. equivalent von Mises strain, equivalent von Mises stress, dislocation density, KAM, and Taylor factor) at the mid-surface of the RVE after a 20% thickness reduction ($\varepsilon = 0.22$). Non-crystallographic band-like deformation regions with large strain accumulation that appear as river-like patterns are formed during the deformation, which pass through several grains and extend across the specimen (see Fig. 9a). The local strain in these regions is, on average, around two times higher than the applied strain. These macroscopic bands are initially formed at an approximate angle of $\pm 40^\circ - 45^\circ$ with the rolling direction. The accumulation of the plastic strain in these macroscopic river-like patterns results in a significantly lower plastic strain in the neighboring regions.

One of the factors that promote such macroscopic strain localization is the mechanical contrast in the plastic behavior among neighboring grains (e.g. yield stress). Strain localization typically initiates near grain boundaries of soft grains with low strain hardening rates. The formation of an area plastically deformed decreases the effective load capacity of the sheared section and results in local mechanical instability. Consequently, the strain localization propagates through the specimen and creates the river-like patterns. The sharpness of the river-like patterns is higher when the contrast in the deformation behavior of the grains is larger (see

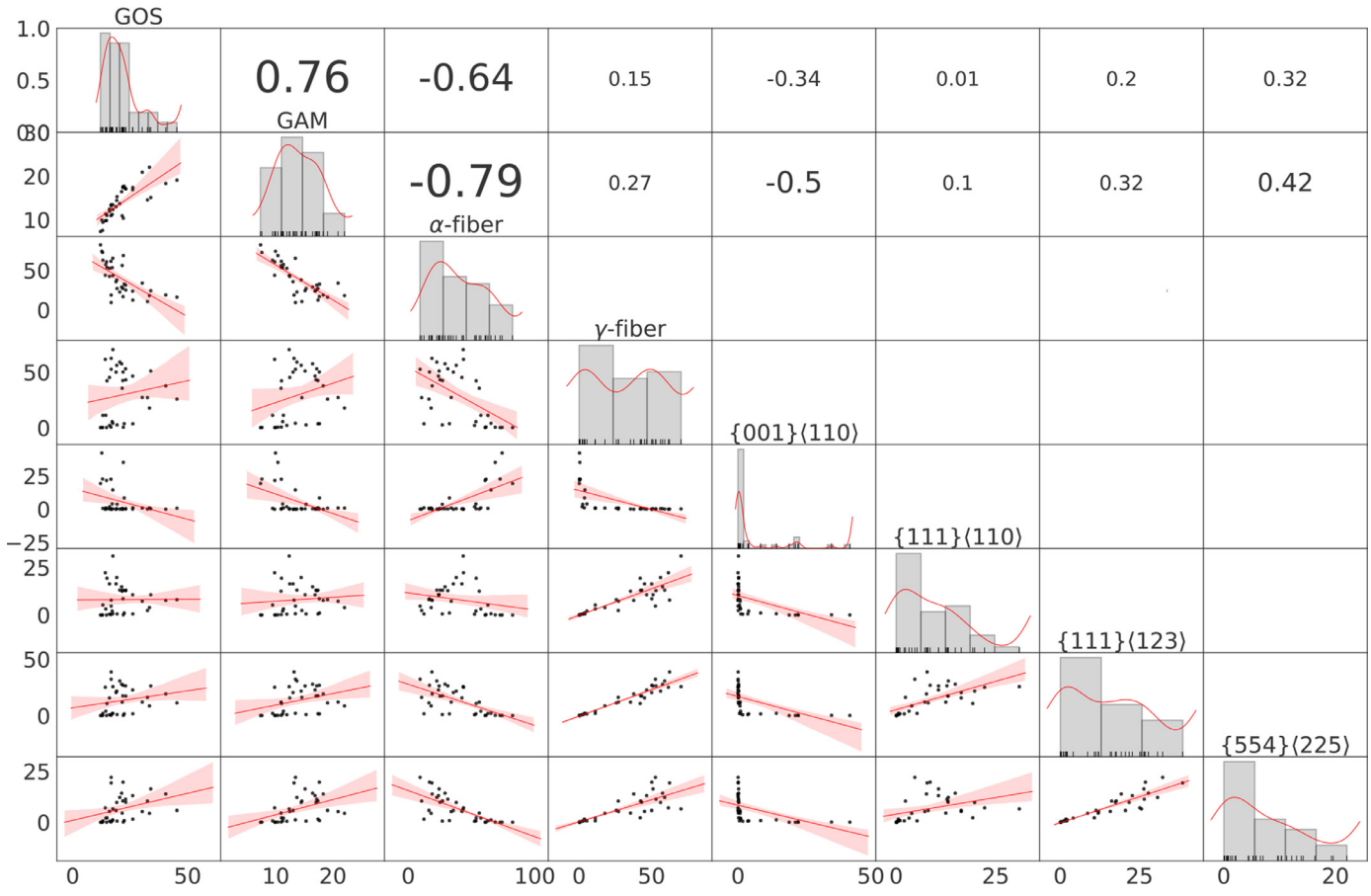

Fig. 7. Correlation matrix showing the dependence between different pairs of variables. The subplots show a scatter plot of a pair of variables with a linear regression fit. The displayed values present the correlation coefficient between the GOS and GAM with volume fraction of various texture components. Each diagonal subplot contains the distribution of a variable as a histogram.

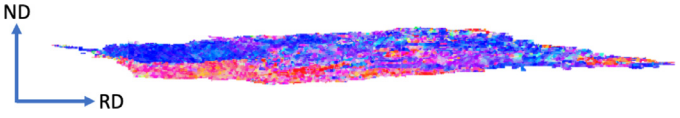

Fig. 8. A 2D section showing the IPF color maps parallel to the loading (ND) direction at the mid-surface of grain 2.

region A1). However, a cluster of soft grains close to the areas of strain localization results in the broadening and homogenizing of the river-like patterns (see region A2). The high deformation concentration at these bands leads to a significantly lower strain in the surrounding regions. For example, for the grain shown in region A1, the strain in the rest of the soft grain is notably small.

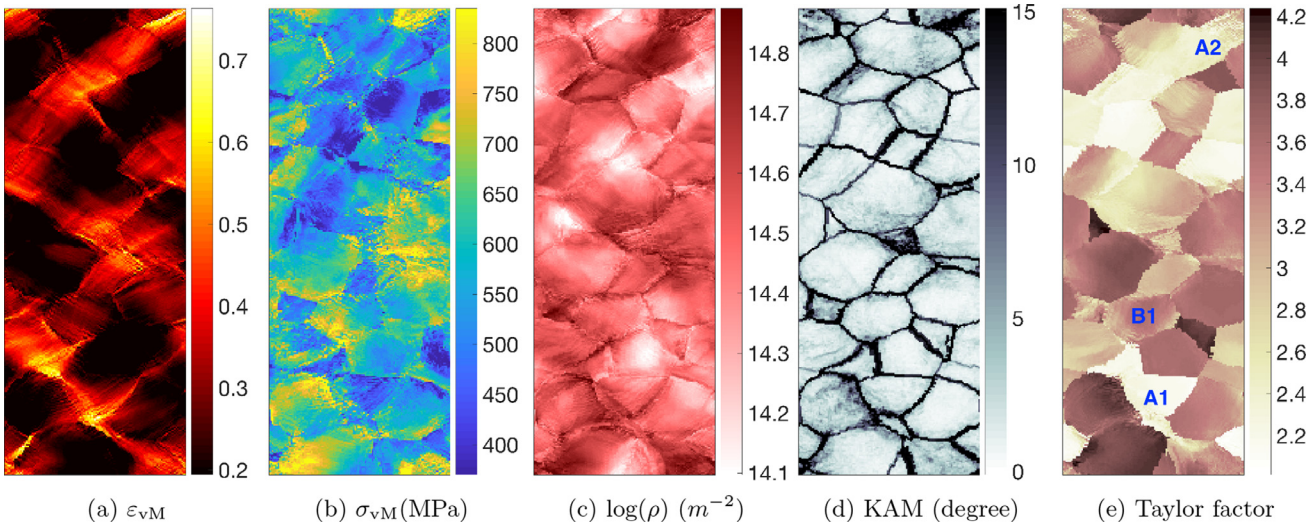

Fig. 9. Simulation results at the mid-surface after a 20% thickness reduction; (a) equivalent strain ε_{vM}, (b) equivalent stress σ_{vM}(MPa), (c) log(ρ) (m^{-2}), (d) KAM (degree), (e) Taylor factor with respect to the loading (vertical) direction.

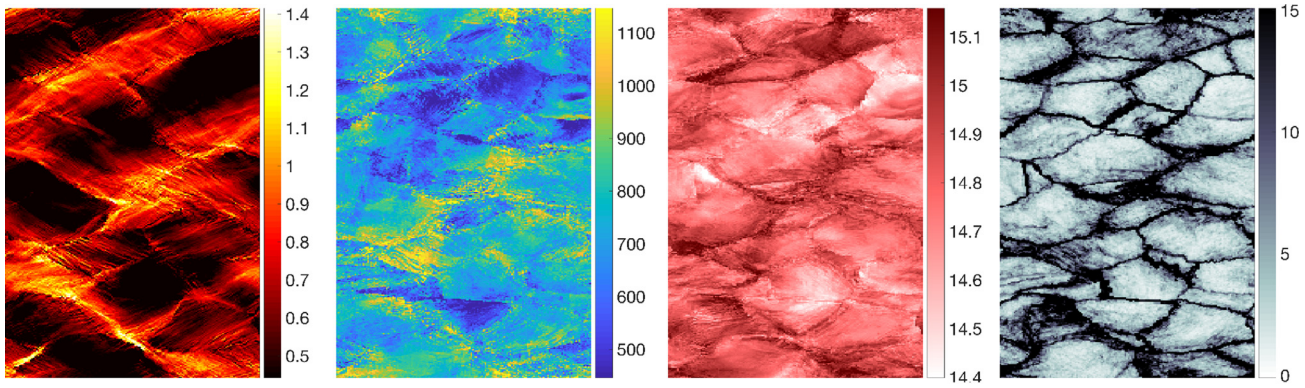

Fig. 10. Simulation results at the mid-surface after a 40% thickness reduction; (a) equivalent strain $\varepsilon_{\mathrm{vM}}$, (b) equivalent stress σ_{vM}(MPa), (c) $\log(\rho)$ (m^{-2}), (d) KAM (degree).

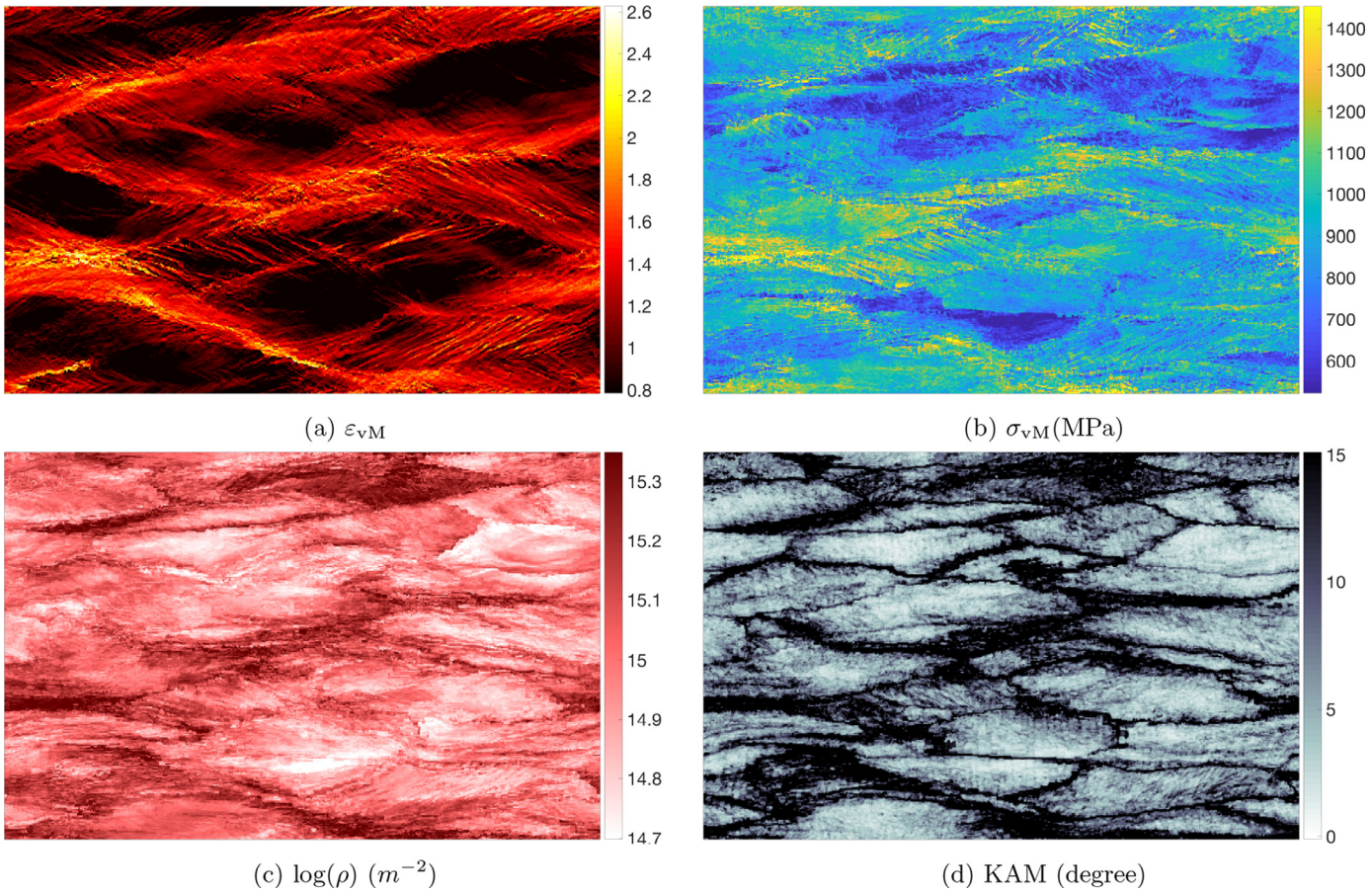

Fig. 11. Simulation results at the mid-surface after a 60% thickness reduction; (a) equivalent strain $\varepsilon_{\mathrm{vM}}$, (b) equivalent stress σ_{vM}(MPa), (c) $\log(\rho)$ (m^{-2}), (d) KAM (degree).

In addition to the river-like patterns which pass through several grains, a small number of rather sharp and highly localized in-grain shear bands can also be observed. These bands extend inside a single grain, and it seems that they originate at the grain boundaries (see region B1). They exist only in a very limited number of grains at this strain level and have developed mainly in hard grains, interrupting the macroscopic river-like patterns. They are formed at an angle of approximately $\pm 30^{\circ} - 35^{\circ}$ with the rolling direction.

The stress values are generally higher in harder grains, i.e. orientations with higher Taylor factor. However, the macroscopic river-like patterns affect the stress distribution inside soft and hard grains considerably. The regions with high stress are mainly located inside hard grains next to the river-like patterns. The in-grain deformation also influences the stress distribution inside the grain. In general, the average stress inside grains with such features is notably higher than the total average stress.

With an increase of thickness reduction to 40% ($\varepsilon = 0.51$), the river-like patterns rotate down to inclination angles of $\pm 30^{\circ} - 35^{\circ}$ to the rolling direction (Fig. 10). In addition, the contrast between the strain in areas with large strain accumulation and the surrounding regions increases, which results in sharper river-like patterns. On the other hand, the in-grain shear bands are more clearly visible, and they develop in a larger number of grains. These bands

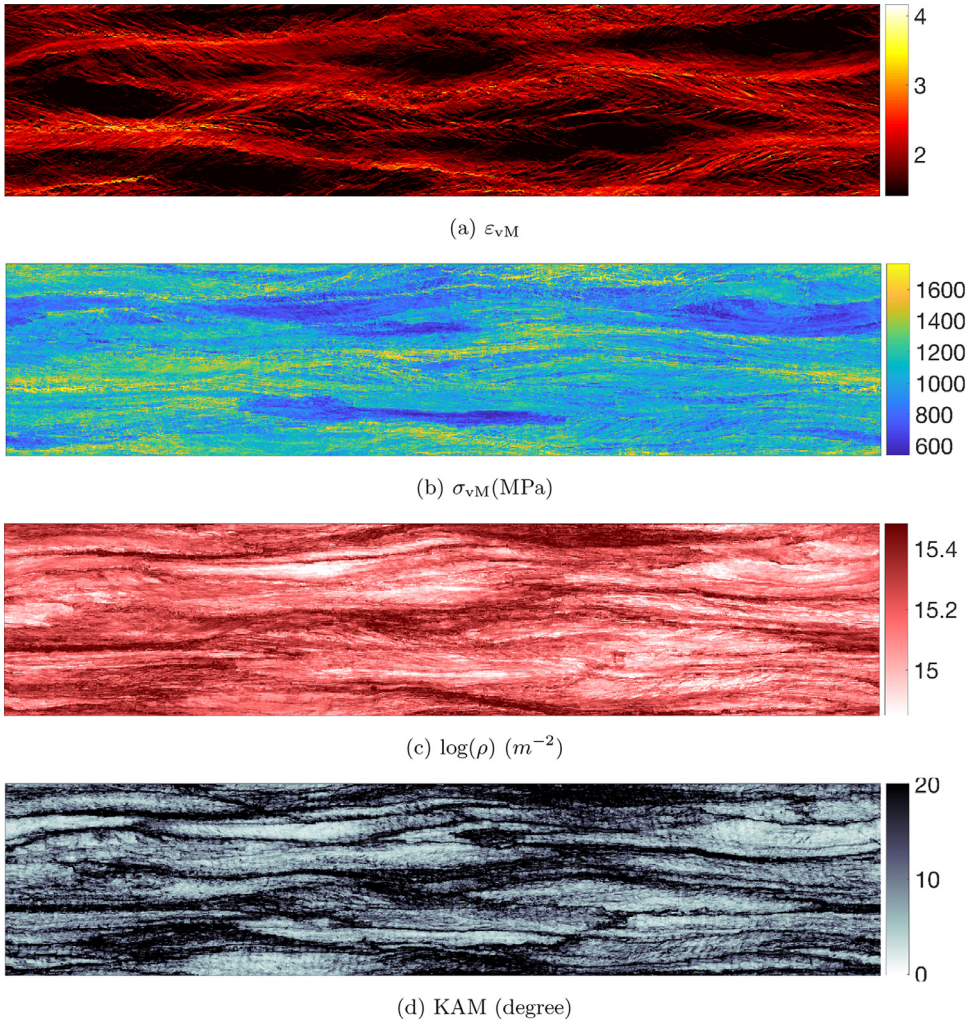

Fig. 12. Simulation results at the mid-surface after a 77% thickness reduction; (a) equivalent strain $\varepsilon_{\mathrm{vM}}$, (b) equivalent stress σ_{vM}(MPa), (c) log(ρ) (m^{-2}), (d) KAM (degree).

still have an angle of around $\pm 30^{\circ} - 35^{\circ}$ with the rolling direction, so unlike the river-like patterns, they do not rotate notably towards the rolling direction. The grains that contain such microstructure features pertain mostly to the γ-fiber.

After 60% thickness reduction ($\varepsilon = 0.92$), the river-like patterns rotate significantly towards inclination angles of $\pm 15^{\circ} - 20^{\circ}$ to the rolling direction (Fig. 11). On the other hand, the angle for the in-grain shear bands is still around $\pm 30^{\circ} - 35^{\circ}$, revealing that the inclination of in-grain shear bands is not noticeably dependent on the applied strain. After 60% thickness reduction, the in-grain shear bands are well developed and established in some grains that mainly belong to the γ-fiber.

After 77% thickness reduction ($\varepsilon = 1.47$), the whole microstructure is severely deformed, and it is difficult to trace the original grain boundaries (Fig. 12). However, it is still possible to identify and trace some of the features previously observed at lower strains. The river-like patterns rotate further towards the rolling direction. In some places, they rotate to inclination angles of $\pm 5^{\circ} - 10^{\circ}$ to the rolling direction, while in some other places, they are almost parallel to the rolling direction. The localized strain in the river-like patterns can reach a value of 4.0, around three times higher than the applied strain.

The in-grain shear bands also rotate slightly, and their inclination angle with the rolling direction rotates to around $\pm 25^{\circ} - 30^{\circ}$. However, bands with an angle of around $\pm 15^{\circ}$ are also observed. The highly rotated in-grain shear bands are mainly those developed at the early stages of deformation, i.e. those already visible at 20% thickness reduction. Moreover, the fraction of in-grain shear bands has increased notably with increasing deformation. The in-grain shear bands are orientation-dependent, i.e. they form preferentially in γ-fiber (high Taylor factor) grains. However, not all grains belonging to the γ-fiber contain such features. Similar experimental observations have been reported for steels [50,55,73].

A 3D view of the river-like patterns after 60% and 77% thickness reductions is shown in Fig. 13a and c, respectively. These patterns are aligned parallel to the transverse direction and extended through the depth of the RVE. Since these macroscopic band-like areas pass through several grains and extend across the specimen, they are comprised of regions belonging to both, the α-fiber and γ-fiber. The regions belonging to the γ-fiber are areas with relatively high local misorientations and stress. On the contrary, regions belonging to the α-fiber deform relatively homogeneous, and their stress value is relatively low. Therefore, the orientations belonging to the γ-fiber have significantly higher stored energy and misorientation than the α-fiber orientations. This facilitates the growth of recrystallized volumes of γ-fiber orientations, i.e. these areas act as successful nucleation sites for recrystallization. This leads to the well-known γ-fiber recrystallization texture appearing after annealing of the cold-rolled IF-steel sheet [6,51,54].

Fig. 14 shows the in-grain shear bands developed in a selected grain, i.e. grain number 24 (see Fig. 5b). It can be seen that the orientation inside the in-grain shear bands is displaced from the ma-

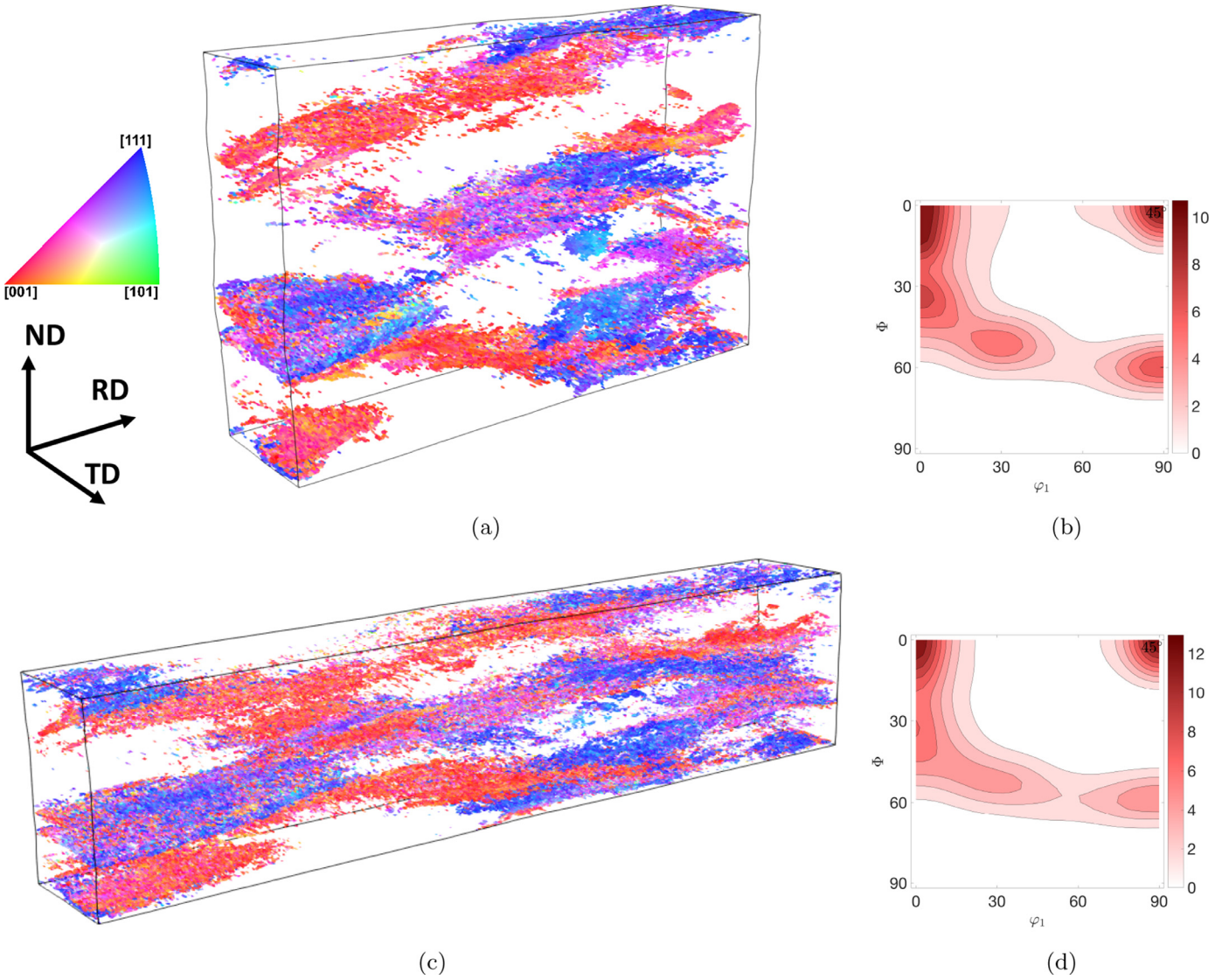

Fig. 13. IPF color maps parallel to the loading (vertical) direction for the river-like patterns after (a) 60% thickness reduction and (c) 77% thickness reductions. The corresponding orientation density f(g) maps ($\varphi_2 = 45^\circ$) after (b) 60% thickness reduction and (d) 77% thickness reductions.

trix orientation of {111}⟨112⟩ toward the orientation of {554}⟨225⟩. This supports the role of in-grain shear bands in the nucleation of the {554}⟨225⟩ recrystallization texture appearing after annealing of the cold-rolled IF-steel sheet [54,62].

Fig. 15 a shows the evolution of the average equivalent strain with deformation in major texture components. The mean equivalent strain is larger in grains with smaller Taylor factors, i.e. orientations close to the rotated cube component. The mean equivalent strain decreases in orientations belonging to the γ-fiber, i.e. orientations with larger Taylor factors.

Fig. 15 b compares the cumulative distributions of equivalent strain (the probability of strain being below a certain value) in major texture components. The figure illustrates the data for all elements after 77% thickness reduction. In addition to the notable difference in the median values, there is a significant difference between the distribution range for different texture components. The median value of the distributions decreases with an increase in the orientation's hardness. The lower bound of the distributions also follows almost the same trend as the median values. However, the upper bounds are not orientation-dependent; it is almost the same for all orientations. This leads to a narrower distribution for the soft grains, i.e. orientations close to the rotated cube component. The distribution becomes wider for orientations further along the α-fiber, and it becomes noticeably wide for hard grains belonging to the γ-fiber. The widest distributions are found for the {111}⟨112⟩ and {111}⟨123⟩ components. This wide distribution is due to the formation of in-grain shear bands in γ-fiber grains. The in-grain shear bands are areas with large strain accumulation. The presence of these bands serves to redistribute plastic strain and significantly reduces the extent of the strain in regions next to these bands, resulting in a large contrast in the strain distribution in these grains.

5.5. Effect of multi-step mesh refinement method

This study uses a multi-step mesh refinement method to adjust the number of elements during the simulation. To further investigate the advantages of this meshing strategy, we have conducted an additional simulation using the same RVE investigated in this section (see Fig. 1a). However, the simulation is performed without using the multi-step mesh refinement method, i.e. the mesh density is kept constant as $80 \times 48 \times 320$. Fig. 16 shows the results after 77% thickness reduction. During the simulation, the element size in the loading direction decreases with increasing the defor-

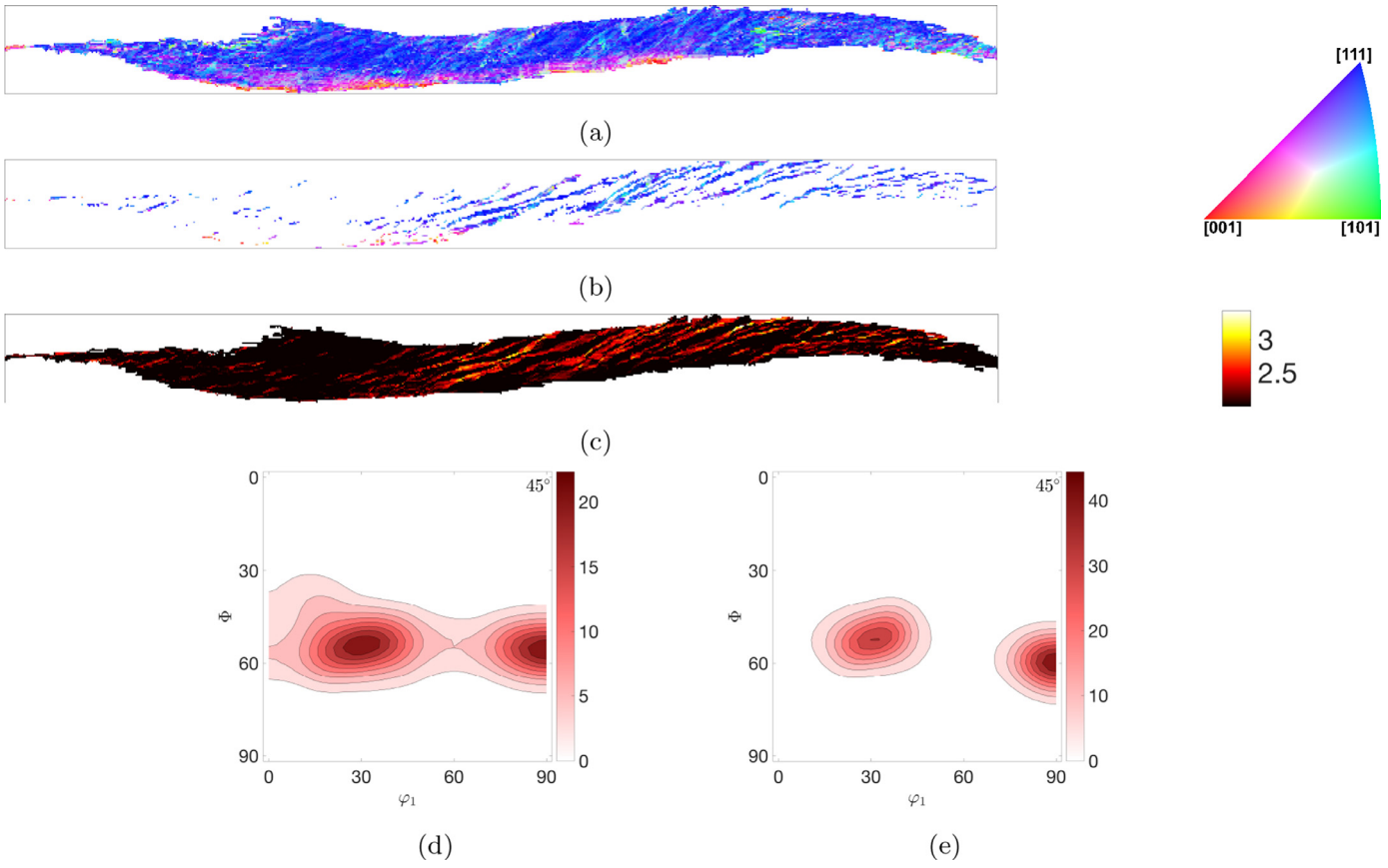

Fig. 14. A 2D section of grain 24 showing IPF color maps parallel to the loading (vertical) direction for (a) the full cross-section, (b) the in-grain shear bands. (c) Strain distribution at the in-grain shear bands. Orientation density f(g) maps obtained from the ODF section $\varphi_2 = 45^\circ$ for the (d) grain matrix and (e) in-grain shear bands.

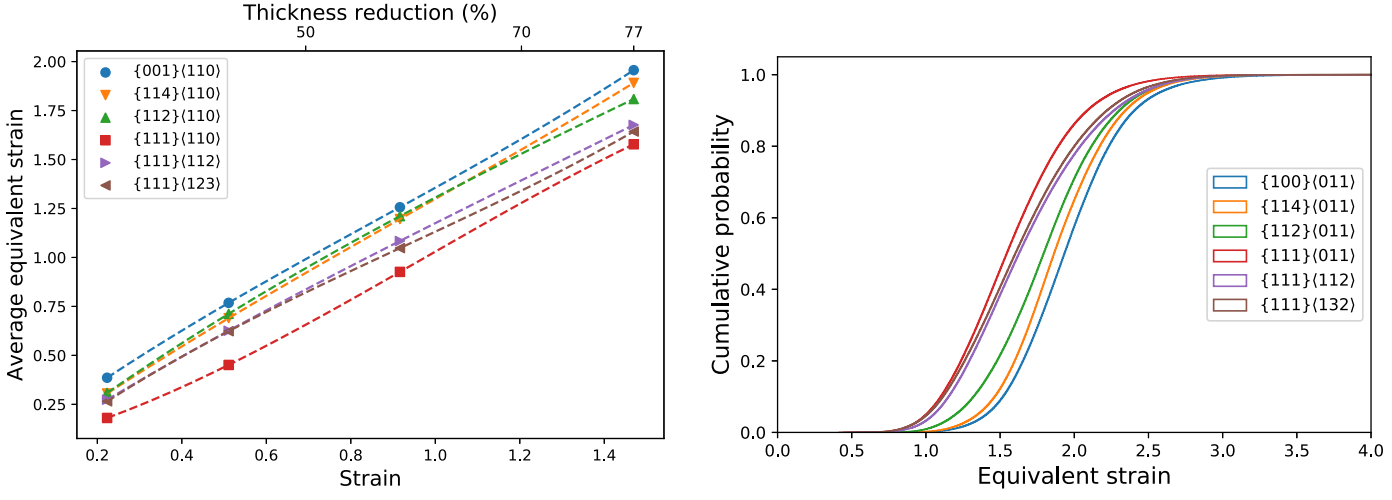

Fig. 15. (a) Evolution of the average equivalent strain with deformation in major texture components. (b) Cumulative distribution of equivalent strain in major texture components after 77% thickness reduction.

mation, while the element is elongated in the stretching (rolling) direction. Therefore, the element becomes rectangular, and the element aspect ratio, the ratio of the element size in the stretching direction to the element size in the compression direction, considerably increases. For this example, the elements' aspect ratio reaches a value around 19 after 77% thickness reductions. An element represents the average response of a section in the discretized space. When the element size is larger than the localized features, it will capture only the homogenized behavior and not the morphology of the localized deformation. Therefore, these elongated elements prevent strain localization from occurring. This behavior can be seen clearly in Fig. 16b, where these highly elongated elements

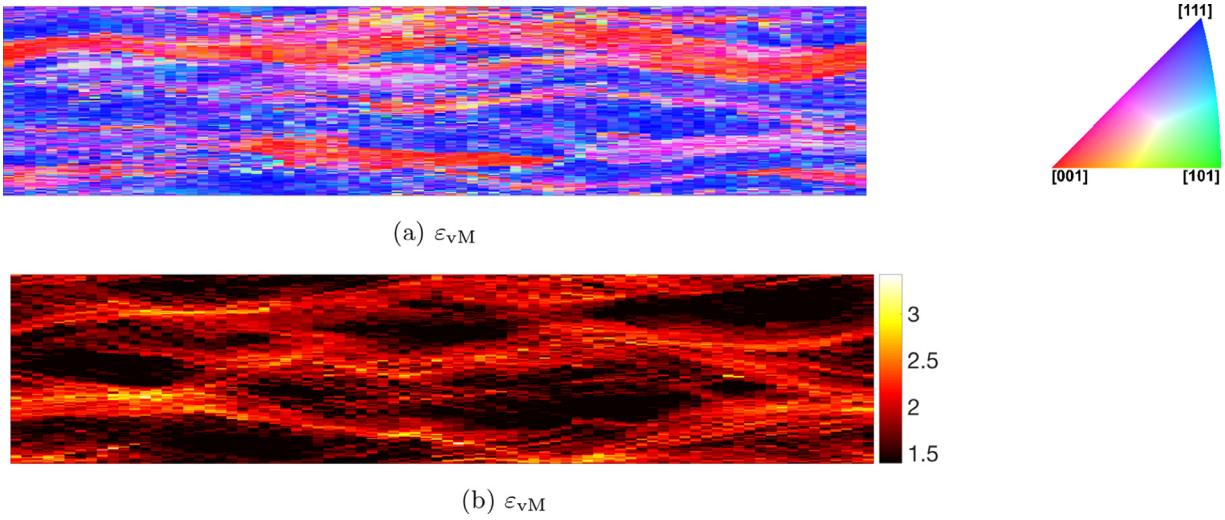

Fig. 16. Simulation results at the mid-surface after 77% thickness reduction; (a) equivalent strain ε_{vM}, (b) equivalent stress σ_{vM}(MPa). The simulation is conducted without using the multi-step mesh refinement method and the mesh density is kept constant as $80 \times 48 \times 320$. Compare with Figs. 1a and 12 a for results including mesh refinement.

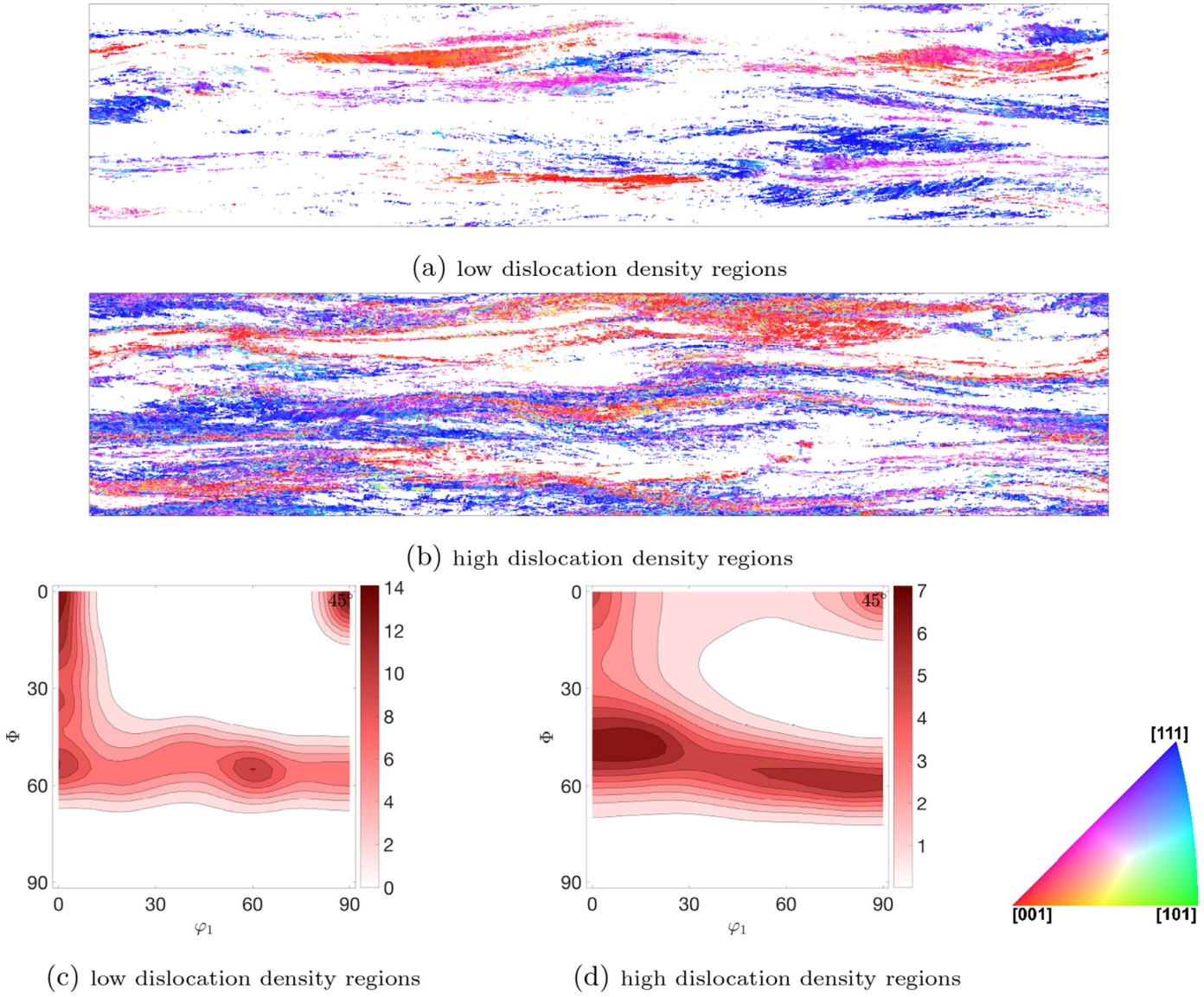

Fig. 17. Simulation results showing low and high dislocation density regions. (a,b) IPF color maps parallel to the loading (vertical) direction, (c,d) orientation density f(g) maps obtained from the ODF section $\varphi_2 = 45^\circ$.

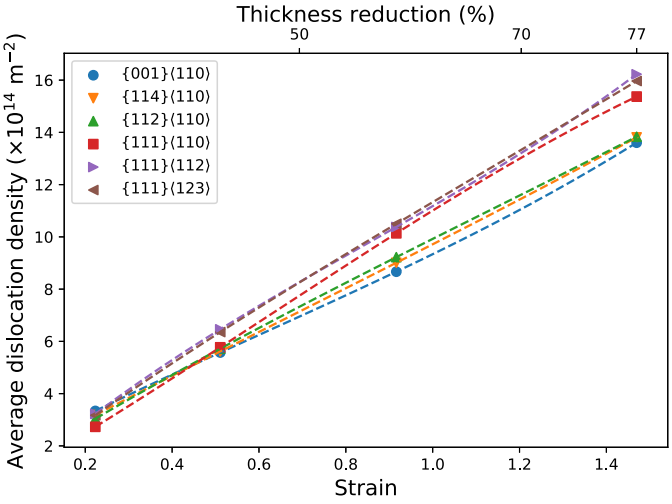

Fig. 18. Average dislocation density in major texture components.

substantially have reduced the level of strain localization. Although the simulation can still capture the global shape of the river-like patterns, it is no longer possible to recognize the details inside and close to these patterns. In addition, it is no longer possible to identify the in-grain shear bands. One should note that the resolution of this simulation (i.e. approximately 3400 elements per grain) is still relatively high compared to typical crystal plasticity simulations. Hence, the use of the multi-step mesh refinement approach is critical for capturing the in-grain microstructure evolution.

5.6. Dislocation density

Orientation dependency of dislocation density

Fig. 17 shows the IPF color map parallel to the loading (vertical) direction at the mid-surface. The data are divided to low dislocation density regions, i.e. points whose dislocation densities belong to the lower 20% of the data distribution, and high dislocation density regions, points whose dislocation densities belong to the higher half of the data distribution. Grains close to the rotated cube component generally have the lowest dislocation density. The dislocation density increases for orientations further along the α-fiber, similar to what was previously observed for KAM. On the other hand, regions that belong to the γ-fiber have the highest dislocation density.

Fig. 18 shows the development of the dislocation density with deformation for major texture components. At 20% thickness reduction, the difference between the dislocation density of different orientations is relatively small. At larger strains, the difference between the dislocation density of γ-fiber and α-fiber components becomes more pronounced. After 77% thickness reduction, the average dislocation density of γ-fiber and α-fiber are 1.45×10^{15} and 1.6×10^{15} m^{-2}, respectively. It should be noted that $\{111\}\langle 110\rangle$ is a common component between γ-fiber and α-fiber. A similar trend for geometrically necessary dislocations (GND) has been reported experimentally, e.g. [55].

Correlation between dislocation density with KAM, ε_{vM}, and σ_{vM}

It is generally accepted that GNDs are related to the in-grain misorientation. Although the crystal plasticity model used here does not differentiate between the GNDs and SSDs (Statistically Stored Dislocations), it is still expected that the total dislocation density correlates with the local misorientation and KAM. Fig. 19a shows the correlation between the dislocation density with other main variables at different strain levels. There is a small positive correlation between the dislocation density and KAM at small strains (0.21). The correlation coefficient increases rapidly, and it reaches a significant value of 0.60 after a 77% thickness reduction. The high correlation value indicates that the dislocation density and the KAM are strongly correlated at large deformation. Fig. 19b shows a 2D probability density plot of the dislocation density and the KAM after 77% thickness reduction.

The correlation between the dislocation density and the equivalent strain follows an opposite trend. There is a strong positive correlation between these two variables at small strains (0.66). However, the correlation coefficient substantially decreases with increasing deformation, and it reduces to 0.13 after 77% thickness reduction. There is a moderate correlation between the equivalent stress and the dislocation density at small strains (0.42). The correlation coefficient steadily increases to 0.58 at 77% thickness reduction.

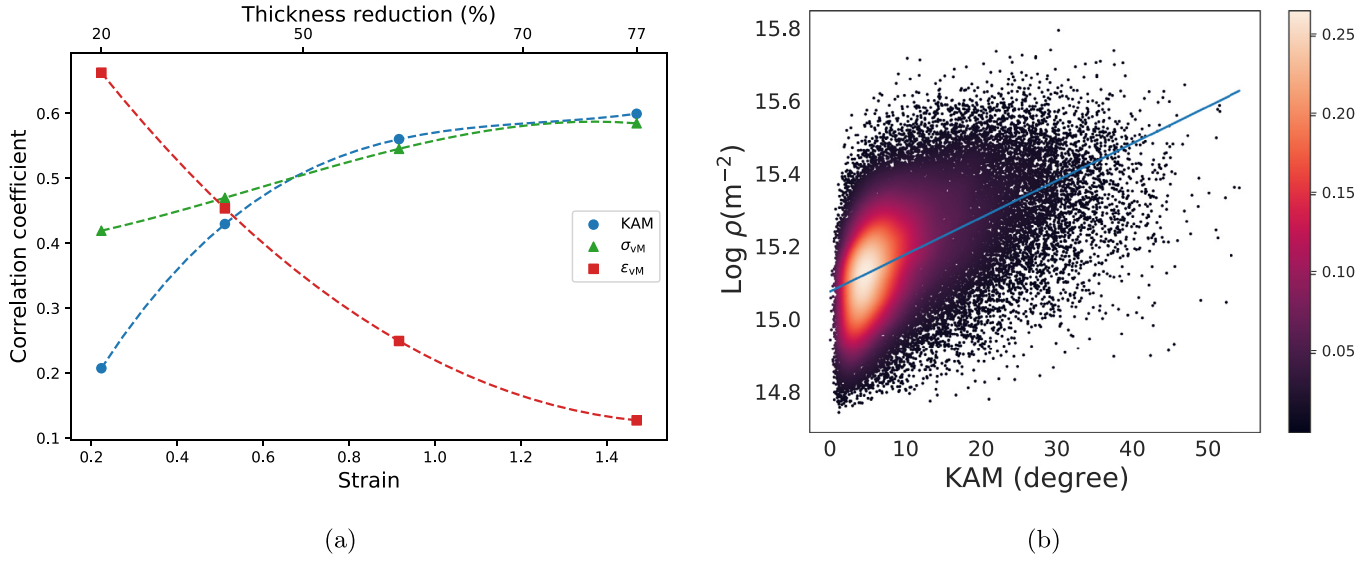

Fig. 19. (a) Correlation between the dislocation density and main variables. (b) 2D probability density plot of the dislocation density and KAM. The blue line shows the linear regression line. (For interpretation of the references to colour in this figure legend, the reader is referred to the web version of this article.)

6. Conclusions

High-resolution 3D crystal plasticity simulations are used to investigate the in-grain microstructural evolution and deformation heterogeneity during large deformation of IF-steel. An RVE consisting of 36 grains is subjected to plane-strain compression up to a thickness reduction of 77%. At this deformation level, around 550000 elements on average are used for the discretization of each grain. The results reveal that the crystallographic orientation of a grain is a critical factor in determining whether a grain deforms relatively homogeneously or heterogeneously. The orientations close to the rotated cube orientation show the minimal tendency to form orientation gradients. The deformation heterogeneity increases for orientations further along the α-fiber. On the other hand, the orientations belonging to the γ-fiber show the strongest misorientation spread.

We observe that band-like areas with severe strain localization extending across the specimen (which appear as river patterns) are formed during deformation. These river-like patterns are initially formed at an approximate angle of $\pm 40^\circ - 45^\circ$ with the rolling direction. With increasing the thickness reduction, the river-like patterns rotate significantly to inclination angles almost parallel to the rolling direction. The localized strain in the river-like patterns can reach a value that is three times the overall applied strain value. In addition to the macroscopic river-like patterns, several regions with rather sharp and highly localized in-grain shear bands are identified. These bands extend inside only one grain. The in-grain shear bands are formed at an angle of approximately $\pm 30^\circ - 35^\circ$ with the rolling direction, and their inclination angle is not noticeably dependent on the applied strain for a wide range of deformation. The in-grain shear bands are orientation-dependent, and they form mainly in grains belonging to the γ-fiber. However, not all grains belonging to the γ-fiber contain such features.

The results reveal that the difference between the dislocation density of different orientations is relatively small at small strains. However, with increasing strain, the dislocation density in the γ-fiber becomes notably larger than in the α-fiber. Although dislocation density and KAM are weakly correlated at small strains, the correlation coefficient increases rapidly with increasing strain. The correlation between the dislocation density and the equivalent strain follows an opposite trend.

Declaration of Competing Interest

The authors declare that they have no known competing financial interests or personal relationships that could have appeared to influence the work reported in this paper.

Acknowledgments

This research was carried out under project number S41.5.15572a in the framework of the Partnership Program of the Materials innovation institute M2i (www.m2i.nl) and the Technology Foundation TTW (www.stw.nl), which is part of the Netherlands Organization for Scientific Research (www.nwo.nl). The industrially cold-rolled IF-steel sample have been provided by Tata Steel Ijmuiden, The Netherlands. The authors are also grateful to Prof. Leo Kestens for helpful discussions.

References

[1] L. Chen, J. Chen, R.A. Lebensohn, Y.Z. Ji, T.W. Heo, S. Bhattacharyya, K. Chang, S. Mathaudhu, Z.K. Liu, L.Q. Chen, An integrated fast fourier transform-based phase-field and crystal plasticity approach to model recrystallization of three dimensional polycrystals, Comput. Method. Appl. Mech. Eng. 285 (2015) 829–848, doi:10.1016/j.cma.2014.12.007.

[2] P. Zhao, T. Song En Low, Y. Wang, S. Niezgoda, An integrated full-field model of concurrent plastic deformation and microstructure evolution: application to 3D simulation of dynamic recrystallization in polycrystalline copper, Int. J. Plast. 80 (2016), doi:10.1016/j.ijplas.2015.12.010.

[3] D. Kim, W. Woo, W. Park, Y. Im, A. Rollett, Mesoscopic coupled modeling of texture formation during recrystallization considering stored energy decomposition, Comput. Mater. Sci 129 (2017), doi:10.1016/j.commatsci.2016.11.048.

[4] K.K. Alaneme, E.A. Okotete, Recrystallization mechanisms and microstructure development in emerging metallic materials: A review, 2019, (????). 10.1016/j.jsamd.2018.12.007

[5] M. Diehl, M. Kühbach, Coupled experimental-computational analysis of primary static recrystallization in low carbon steel, Modell. Simul. Mater. Sci. Eng. 28 (1) (2020), doi:10.1088/1361-651X/ab51bd.

[6] K. Traka, K. Sedighiani, C. Bos, J. Galan Lopez, K. Angenendt, D. Raabe, J. Sietsma, Topological aspects responsible for recrystallization evolution in an IF-steel sheet investigation with cellular-automaton simulations, Comput. Mater. Sci 198 (2021) 110643, doi:10.1016/j.commatsci.2021.110643.

[7] V. Shah, K. Sedighiani, J. Van Dokkum, C. Bos, F. Roters, M. Diehl, Coupling crystal plasticity and cellular automaton models to study meta-dynamic recrystallization during hot rolling at high strain rates, Mater. Sci. Eng. 849 (2022) 143471, doi:10.1016/j.msea.2022.143471.

[8] C.C. Tasan, J.P.M. Hoefnagels, M. Diehl, D. Yan, F. Roters, D. Raabe, Strain localization and damage in dual phase steels investigated by coupled in-situ deformation experiments and crystal plasticity simulations, Int. J. Plast. 63 (2014) 198–210, doi:10.1016/j.ijplas.2014.06.004.

[9] M. Diehl, M. Wicke, P. Shanthraj, F. Roters, A. Brueckner-Foit, D. Raabe, Coupled crystal plasticityphase field fracture simulation study on damage evolution around a void: pore shape versus crystallographic orientation, Jom 69 (5) (2017) 872–878, doi:10.1007/s11837-017-2308-8.

[10] H. Hallberg, S.K. Ås, B. Skallerud, Crystal plasticity modeling of microstructure influence on fatigue crack initiation in extruded al6082-T6 with surface irregularities, Int. J. Fatigue 111 (2018), doi:10.1016/j.ijfatigue.2018.01.025.

[11] H.S. Oh, K. Biggs, O. Güvenç, H. Ghassemi-Armaki, N. Pottore, C.C. Tasan, In-situ investigation of strain partitioning and microstructural strain path development up to and beyond necking, Acta Mater. 215 (2021), doi:10.1016/j.actamat.2021.117023.

[12] E.K. Cerreta, I.J. Frank, G.T. Gray, C.P. Trujillo, D.A. Korzekwa, L.M. Dougherty, The influence of microstructure on the mechanical response of copper in shear, Mater. Sci. Eng. A 501 (1–2) (2009), doi:10.1016/j.msea.2008.10.029.

[13] G. Zhou, M.K. Jain, P. Wu, Y. Shao, D. Li, Y. Peng, Experiment and crystal plasticity analysis on plastic deformation of AZ31B Mg alloy sheet under intermediate temperatures: how deformation mechanisms evolve, Int. J. Plast. 79 (2016), doi:10.1016/j.ijplas.2015.12.006.

[14] A.J. Beaudoin, H. Mecking, U.F. Kocks, Development of localized orientation gradients in fcc polycrystals, Philosophical Magazine A: Physics of Condensed Matter, Structure, Defects and Mechanical Properties 73 (6) (1996), doi:10.1080/01418619608242998.

[15] M. Sachtleber, Z. Zhao, D. Raabe, Experimental investigation of plastic grain interaction, Mater. Sci. Eng., A 336 (1–2) (2002) 81–87, doi:10.1016/S0921-5093(01)01974-8.

[16] D. Raabe, Z. Zhao, F. Roters, Study on the orientational stability of cube-oriented FCC crystals under plane strain by use of a texture component crystal plasticity finite element method, Scr. Mater. 50 (7) (2004), doi:10.1016/j.scriptamat.2003.11.061.

[17] K.S. Cheong, E.P. Busso, Effects of lattice misorientations on strain heterogeneities in FCC polycrystals, J. Mech. Phys. Solid. 54 (4) (2006), doi:10.1016/j.jmps.2005.11.003.

[18] C. Zhang, H. Li, P. Eisenlohr, W. Liu, C.J. Boehlert, M.A. Crimp, T.R. Bieler, Effect of realistic 3D microstructure in crystal plasticity finite element analysis of polycrystalline ti-5Al-2.5Sn, Int. J. Plast. 69 (2015), doi:10.1016/j.ijplas.2015.01.003.

[19] J. Oddershede, J.P. Wright, A. Beaudoin, G. Winther, Deformation-induced orientation spread in individual bulk grains of an interstitial-free steel, Acta Mater. 85 (2015), doi:10.1016/j.actamat.2014.11.038.

[20] D. Wang, M. Diehl, F. Roters, D. Raabe, On the role of the collinear dislocation interaction in deformation patterning and laminate formation in single crystal plasticity, Mech. Mater. 125 (2018), doi:10.1016/j.mechmat.2018.06.007.

[21] J. Cappola, J.C. Stinville, M. Charpagne, P.G. Callahan, M.P. Echlin, T.M. Pollock, A. Pilchak, M. Kasemer, On the localization of plastic strain in microtextured regions of Ti-6Al-4V, Acta Mater. 204 (2021) 116492, doi:10.1016/j.actamat.2020.116492.

[22] S.H. Choi, Y.S. Jin, Evaluation of stored energy in cold-rolled steels from EBSD data, Mater. Sci. Eng., A 371 (1–2) (2004), doi:10.1016/j.msea.2003.11.034.

[23] S.H. Choi, J.H. Cho, Primary recrystallization modelling for interstitial free steels, Mater. Sci. Eng., A 405 (1–2) (2005), doi:10.1016/j.msea.2005.05.093.

[24] S. Zaefferer, N.-N. Elhami, P. Konijnenberg, Electron backscatter diffraction (EBSD) techniques for studying phase transformations in steels, Phase Transform. Steel. (2012) 557–587, doi:10.1533/9780857096111.4.557.

[25] N. Allain-Bonasso, F. Wagner, S. Berbenni, D.P. Field, A study of the heterogeneity of plastic deformation in IF steel by EBSD, Mater. Sci. Eng., A 548 (2012), doi:10.1016/j.msea.2012.03.068.

[26] S. Wang, Z.H. Wu, C. Chen, S.K. Feng, R. Liu, B. Liao, Z.H. Zhong, P. Lu, M.P. Wang, P. Li, J.W. Coenen, L.F. Cao, Y.C. Wu, The evolution of shear bands in Ta-2.5W alloy during cold rolling, Mater. Sci. Eng., A 726 (2018), doi:10.1016/j.msea.2018.04.059.

[27] B.L. Li, A. Godfrey, Q.C. Meng, Q. Liu, N. Hansen, Microstructural evolution of IF-steel during cold rolling, Acta Mater. 52 (4) (2004) 1069–1081, doi:10.1016/j.actamat.2003.10.040.

[28] D.A. Hughes, N. Hansen, The microstructural origin of work hardening stages, Acta Mater. 148 (2018), doi:10.1016/j.actamat.2018.02.002.
[29] F. Roters, P. Eisenlohr, L. Hantcherli, D.D. Tjahjanto, T.R. Bieler, D. Raabe, Overview of constitutive laws, kinematics, homogenization and multiscale methods in crystal plasticity finite-element modeling: theory, experiments, applications, Acta Mater. 58 (4) (2010) 1152–1211, doi:10.1016/j.actamat.2009.10.058.
[30] C. Reuber, P. Eisenlohr, F. Roters, D. Raabe, Dislocation density distribution around an indent in single-crystalline nickel : comparing nonlocal crystal plasticity finite-element predictions with experiments, Acta Mater. 71 (2014) 333–348, doi:10.1016/j.actamat.2014.03.012.
[31] M. Khadyko, S. Dumoulin, O.S. Hopperstad, Texture gradients and strain localisation in extruded aluminium profile, Int. J. Solid. Struct. 97_98 (2016) 239–255, doi:10.1016/j.ijsolstr.2016.07.024.
[32] M. Diehl, D. An, P. Shanthraj, S. Zaefferer, F. Roters, D. Raabe, Crystal plasticity study on stress and strain partitioning in a measured 3D dual phase steel microstructure, Phys. Mesomech. 20 (3) (2017a), doi:10.1134/S1029959917030079.
[33] M. Diehl, M. Groeber, C. Haase, D.A. Molodov, F. Roters, D. Raabe, Identifying structureproperty relationships through DREAM.3D representative volume elements and DAMASK crystal plasticity simulations: an integrated computational materials engineering approach, JOM 69 (5) (2017b), doi:10.1007/s11837-017-2303-0.
[34] H. Zhang, J. Liu, D. Sui, Z. Cui, M.W. Fu, Study of microstructural grain and geometric size effects on plastic heterogeneities at grain-level by using crystal plasticity modeling with high-fidelity representative microstructures, Int. J. Plast. 100 (2018), doi:10.1016/j.ijplas.2017.09.011.
[35] M. Diehl, J. Niehuesbernd, E. Bruder, Quantifying the contribution of crystallographic texture and grain morphology on the elastic and plastic anisotropy of bcc steel, Metals (Basel) 9 (12) (2019), doi:10.3390/met9121252.
[36] T.F. van Nuland, J.A. van Dommelen, M.G. Geers, Microstructural modeling of anisotropic plasticity in large scale additively manufactured 316l stainless steel, Mech. Mater. 153 (2021), doi:10.1016/j.mechmat.2020.103664.
[37] J.L. Dequiedt, C. Denoual, Localization of plastic deformation in stretching sheets with a crystal plasticity approach: competition between weakest link and instable mode controlled process, Int. J. Solid. Struct. 210–211 (2021), doi:10.1016/j.ijsolstr.2020.11.021.
[38] D. Raabe, M. Sachtleber, Z. Zhao, F. Roters, S. Zaefferer, Micromechanical and macromechanical effects in grain scale polycrystal plasticity experimentation and simulation, Acta Mater. 49 (17) (2001) 3433–3441, doi:10.1016/S1359-6454(01)00242-7.
[39] K. Thool, A. Patra, D. Fullwood, K. Krishna, D. Srivastava, I. Samajdar, The role of crystallographic orientations on heterogeneous deformation in a zirconium alloy: a combined experimental and modeling study, Int. J. Plast. 133 (2020), doi:10.1016/j.ijplas.2020.102785.
[40] S. Zaefferer, J.C. Kuo, Z. Zhao, M. Winning, D. Raabe, On the influence of the grain boundary misorientation on the plastic deformation of aluminum bicrystals, Acta Mater. 51 (16) (2003), doi:10.1016/S1359-6454(03)00259-3.
[41] A. Ma, F. Roters, D. Raabe, A dislocation density based constitutive model for crystal plasticity FEM including geometrically necessary dislocations, Acta Mater. 54 (8) (2006a) 2169–2179, doi:10.1016/j.actamat.2006.01.005.
[42] A. Ma, F. Roters, D. Raabe, On the consideration of interactions between dislocations and grain boundaries in crystal plasticity finite element modeling theory, experiments, and simulations, Acta Mater. 54 (8) (2006b) 2181–2194, doi:10.1016/j.actamat.2006.01.004.
[43] C. Rehrl, B. Völker, S. Kleber, T. Antretter, R. Pippan, Crystal orientation changes: a comparison between a crystal plasticity finite element study and experimental results, Acta Mater. 60 (5) (2012), doi:10.1016/j.actamat.2011.12.052.
[44] K. Sedighiani, V. Shah, K. Traka, M. Diehl, F. Roters, J. Sietsma, D. Raabe, Large-deformation crystal plasticity simulation of microstructure and microtexture evolution through adaptive remeshing, Int. J. Plast. 146 (May) (2021) 103078, doi:10.1016/j.ijplas.2021.103078.
[45] D.K. Kim, J.M. Kim, W.W. Park, H. Lee, Y.T. Im, Y.S. Lee, Three-dimensional crystal plasticity finite element analysis of microstructure and texture evolution during channel die compression of if steel, Comput. Mater. Sci 100 (PA) (2015) 52–60, doi:10.1016/j.commatsci.2014.09.032.
[46] H. Lim, C.C. Battaile, J.E. Bishop, J.W. Foulk, Investigating mesh sensitivity and polycrystalline RVEs in crystal plasticity finite element simulations, Int. J. Plast. 121 (2019) 101–115, doi:10.1016/j.ijplas.2019.06.001.
[47] M. Rhee, H.M. Zbib, J.P. Hirth, H. Huang, T. De La Rubia, Models for long-/short-range interactions and cross slip in 3D dislocation simulation of BCC single crystals, Modell. Simul. Mater. Sci. Eng. 6 (4) (1998), doi:10.1088/0965-0393/6/4/012.
[48] A. Patra, D. McDowell, Crystal plasticity-based constitutive modelling of irradiated bcc structures, Philos. Mag. 92 (7) (2012) 861–887, doi:10.1080/14786435.2011.634855.
[49] D. Raabe, K. Luecke, Rolling and annealing textures of bcc metals, Mater. Sci. Forum 157-6 (pt 1) (1994), doi:10.4028/www.scientific.net/msf.157-162.597.
[50] M.R. Barnett, J.J. Jonas, Influence of ferrite rolling temperature on microstructure and texture in deformed low c and IF steels, ISIJ Int. 37 (7) (1997), doi:10.2355/isijinternational.37.697.
[51] B. Hutchinson, Deformation microstructures and textures in steels, Philosoph. Transact. Roy. Soc. 357 (1756) (1999) 1471–1485, doi:10.1098/rsta.1999.0385.
[52] D. Raabe, Z. Zhao, S.J. Park, F. Roters, Theory of orientation gradients in plastically strained crystals, Acta Mater. 50 (2) (2002), doi:10.1016/S1359-6454(01)00323-8.
[53] P. Van Houtte, S. Li, M. Seefeldt, L. Delannay, Deformation texture prediction: from the Taylor model to the advanced Lamel model, Int. J. Plast. 21 (3) (2005) 589–624, doi:10.1016/j.ijplas.2004.04.011.
[54] L.A.I. Kestens, H. Pirgazi, Texture formation in metal alloys with cubic crystal structures, Mater. Sci. Technol. 32 (13) (2016) 1303–1315, doi:10.1080/02670836.2016.1231746.
[55] N. Deeparekha, A. Gupta, M. Demiral, R.K. Khatirkar, Cold rolling of an interstitial free (IF) steelexperiments and simulations, Mech. Mater. 148 (2020), doi:10.1016/j.mechmat.2020.103420.
[56] R. Pokharel, J. Lind, A.K. Kanjarla, R.A. Lebensohn, S.F. Li, P. Kenesei, R.M. Suter, A.D. Rollett, Polycrystal plasticity: comparison between grain - scale observations of deformation and simulations, Annu. Rev. Condens. Matter Phys. 5 (1) (2014), doi:10.1146/annurev-conmatphys-031113-133846.
[57] Q.Z. Chen, B.J. Duggan, On cells and microbands formed in an interstitial-free steel during cold rolling at low to medium reductions, Metall. Mater. Trans. A 35 A (11) (2004), doi:10.1007/s11661-004-0178-5.
[58] D. Vanderschueren, N. Yoshinaga, K. Koyama, Recrystallisation of ti IF steel investigated with electron back-scattering pattern (EBSP), ISIJ Int. 36 (8) (1996) 1046–1054, doi:10.2355/isijinternational.36.1046.
[59] P. Van Houtte, L. Delannay, I. Samajdar, Quantitative prediction of cold rolling textures in low-Carbon steel by means of the Lamel model, Textures and Microstructures 31 (3) (1999) 109–149, doi:10.1155/tsm.31.109.
[60] J. Gil Sevillano, P. van Houtte, E. Aernoudt, Large strain work hardening and textures, 1980, (????). 10.1016/0079-6425(80)90001-8
[61] M. Hatherly, A.S. Malin, Shear bands in deformed metals, Scr. Metall. 18 (5) (1984), doi:10.1016/0036-9748(84)90419-8.
[62] M.R. Barnett, Role of in-grain shear bands in the nucleation of 111 //ND recrystallization textures in warm rolled steel, ISIJ Int. 38 (1) (1998), doi:10.2355/isijinternational.38.78.
[63] K. Ushioda, W.B. Hutchinson, Role of shear bands in annealing texture formation in 3%Si-Fe (111)[112] single crystals, ISIJ Int. 29 (10) (1989), doi:10.2355/isijinternational.29.862.
[64] W.B. Lee, K.C. Chan, Symmetry requirement in shear band formation, Scripta Metallurgica et Materiala 24 (6) (1990), doi:10.1016/0956-716X(90)90289-S.
[65] K. Sedighiani, K. Traka, F. Roters, D. Raabe, J. Sietsma, M. Diehl, Determination and analysis of the constitutive parameters of temperature-dependent dislocation-density-based crystal plasticity models, submitted to Mechanics of Materials (2021).
[66] P. Eisenlohr, F. Roters, Selecting a set of discrete orientations for accurate texture reconstruction, Comput. Mater. Sci 42 (4) (2008), doi:10.1016/j.commatsci.2007.09.015.
[67] P. Eisenlohr, M. Diehl, R. Lebensohn, F. Roters, A spectral method solution to crystal elasto-viscoplasticity at finite strains, Int. J. Plast. 46 (2013) 37–53, doi:10.1016/j.ijplas.2012.09.012.
[68] P. Shanthraj, P. Eisenlohr, M. Diehl, F. Roters, Numerically robust spectral methods for crystal plasticity simulations of heterogeneous materials, Int. J. Plast. 66 (2015) 31–45, doi:10.1016/j.ijplas.2014.02.006.
[69] F. Roters, M. Diehl, P. Shanthraj, P. Eisenlohr, C. Reuber, S. Wong, T. Maiti, A. Ebrahimi, T. Hochrainer, H. Fabritius, S. Nikolov, M. Friák, N. Fujita, N. Grilli, K. Janssens, N. Jia, P. Kok, D. Ma, F. Meier, E. Werner, M. Stricker, D. Weygand, D. Raabe, DAMASK The düsseldorf advanced material simulation kit for modeling multi-physics crystal plasticity, thermal, and damage phenomena from the single crystal up to the component scale, Comput. Mater. Sci 158 (2019) 420–478, doi:10.1016/j.commatsci.2018.04.030.
[70] A. Ma, F. Roters, A constitutive model for fcc single crystals based on dislocation densities and its application to uniaxial compression of aluminium single crystals, Acta Mater. 52 (12) (2004) 3603–3612, doi:10.1016/j.actamat.2004.04.012.
[71] K. Sedighiani, M. Diehl, K. Traka, F. Roters, J. Sietsma, D. Raabe, An efficient and robust approach to determine material parameters of crystal plasticity constitutive laws from macro-scale stressstrain curves, Int. J. Plast. 134 (2020) 102779, doi:10.1016/j.ijplas.2020.102779.
[72] D. Raabe, Investigation of the orientation dependence of recovery in low-carbon steel by use of single orientation determination, Steel Res. 66 (5) (1995), doi:10.1002/srin.199501116.
[73] M. Calcagnotto, D. Ponge, E. Demir, D. Raabe, Orientation gradients and geometrically necessary dislocations in ultrafine grained dual-phase steels studied by 2D and 3D EBSD, Mater. Sci. Eng., A 527 (10–11) (2010), doi:10.1016/j.msea.2010.01.004.